Hydrodynamic and Biochemical Impacts on the Development of Hypoxia in the Louisiana–Texas Shelf Part II: Statistical Modeling and Hypoxia Prediction

Yanda Ou[1] , Bin Li[2], Z. George Xue[1,3,4]

[1]Department of Oceanography and Coastal Sciences, Louisiana State University, Baton Rouge, LA, 70803, USA.

[2]Department of Experimental Statistics, Louisiana State University, Baton Rouge, LA, 70803, USA

[3]Center for Computation and Technology, Louisiana State University, Baton Rouge, LA, 70803, USA.

[4]Coastal Studies Institute, Louisiana State University, Baton Rouge, LA, 70803, USA

Correspondence to: Z. George Xue (zxue@lsu.edu)

Abstract. This study presents a novel ensemble regression model for hypoxic area (HA) forecast in the Louisiana–Texas (LaTex) Shelf. The ensemble model combines a zero-inflated Poisson generalized linear model (GLM) and a quasi-Poisson generalized additive model (GAM) and considers predictors with hydrodynamic and biochemical features. Both models were trained and calibrated using the daily hindcast (2007–2020) by a three-dimensional coupled hydrodynamic–biogeochemical model embedded in the Reginal Ocean Modeling System (ROMS). Compared to the ROMS hindcasts, the ensemble model yields a low root-mean-squared error (RMSE) (3,256 km^2), a high R^2 (0.7721), and low mean absolute percentage biases for overall (29 %) and peak HA prediction (25 %). When compared to the Shelf-wide cruise observations from 2012 to 2020, our ensemble model provides a more accurate summer HA forecast than any existing forecast models with a high R^2 (0.9200), a low RMSE (2,005 km^2), a low scatter index (15 %), and low mean absolute percentage biases for overall (18 %), fair-weather summers (15 %), and windy summers (18 %) predictions. To test its robustness, the model is further applied to a global forecast model and produces HA prediction from 2012 to 2020 with the adjusted predictors from the HYbrid Coordinate Ocean Model (HYCOM). In addition, model sensitivity tests suggest an aggressive riverine nutrient reduction strategy (92 %) is needed to achieve the HA reduction goal of 5,000 km^2.

1 Introduction

The Louisiana–Texas (LaTex) Shelf has become a center of hypoxia (bottom dissolved oxygen, DO<2 mg L^{-1}) study since the 1980s (e.g., Rabalais et al., 2002; Rabalais et al., 2007a; Justić and Wang, 2014). Regular mid-summer Shelf-wide cruises documented that the area and volume of hypoxic bottom water could reach up to 23,000 km^2 and 140 km^3, respectively (Rabalais and Turner, 2019; Rabalais and Baustian, 2020). The aquatic environments, fisheries, and coastal economies are under threat of recurring hypoxia in summer (Chesney and Baltz, 2001; Craig and Bosman, 2013; De Mutsert et al., 2016; LaBone et al., 2020; Rabalais and Turner, 2019; Rabotyagov et al., 2014; Smith et al., 2014). For example, habitats of some fish species (e.g., croaker and brown shrimp) shift to offshore hypoxic edges (Craig and Crowder, 2005; Craig, 2012) during

31 summer hypoxia events, which may impact organism energy budgets and trophic interactions (Craig and Crowder, 2005;
32 Hazen et al., 2009). The horizontal displacement of brown shrimp habitats in summer can also lead to changes in the
33 distribution of Gulf shrimp fleets (Purcell et al., 2017). Although an Action Plan has been launched by the Mississippi
34 River/Gulf of Mexico Hypoxia Task Force to control the size of the mid-summer hypoxic zone below 5,000 km^2 in a 5-year
35 running average since 2001 (Mississippi River/Gulf of Mexico Watershed Nutrient Task Force, 2001; 2008), hypoxic areal
36 extents experience no significant decreases in recent decades (Del Giudice et al., 2020). An accurate prediction of the hypoxic
37 area is urgently needed for coastal managers and the fishery industry.
38
39 Water column stratification and sediment oxygen consumption (SOC) are two main factors regulating the formation, evolution,
40 and destruction of bottom hypoxia from mid-May through mid-September (Bianchi et al., 2010; Conley et al., 2009; Fennel et
41 al., 2011, 2013, 2016; Feng et al., 2014; Hetland and DiMarco, 2008; Justić and Wang, 2014; Laurent et al., 2018; McCarthy
42 et al., 2013; Murrell and Lehrter, 2011; Rabalais et al., 2007b; Wang and Justić, 2009; Yu et al., 2015). The stratification
43 inhibits bottom water reoxygenation, while SOC, induced by water eutrophication associated with high anthropogenic nutrient
44 supplies by rivers, can lead to anaerobic benthic environments. Nevertheless, existing hypoxic area (HA) prediction models
45 rely most on contribution from the nutrient load rather than hydrodynamic features. Turner et al. (2006) built a multiple linear
46 regression model for summer HA prediction using the annual and May nitrogen flux (nitrate+nitrite) of the Mississippi River
47 as the predictors. The model provides a robust annual prediction when no strong wind is present but overestimates the HA in
48 windy years. Obenour et al. (2015) modeled HA using the empirical relationship between HA and bottom DO concentration
49 derived from a Bayesian biophysical model. Their model accounts for primary biophysical processes solved for steady-state
50 conditions, water transport, May total nitrogen loads by rivers, and parameterized water reaeration. Katin et al. (2022) further
51 adjusted the Bayesian model by taking into account river flows, riverine bioavailable nitrogen loadings, and wind velocity in
52 both summer (June–September) and non-summer (November–May) months. Summer riverine inputs are projected using non-
53 summer riverine variables, river basin precipitation, and river basin temperature, while summer wind velocity is resampled
54 from historical records from 1985 to 2016. Therefore, the season prediction model is known as a pseudo-forecast model since
55 predictors in future stages only include riverine inputs. This model explains 71 % and 41 %–48 % of the variability in hindcast
56 (Del Giudice et al., 2020) and geostatistically estimated HA (Matli et al., 2018), respectively. An additional Bayesian model
57 applied to summer bottom DO prediction accounts for May total nitrogen loads, distance from the Mississippi River mouth,
58 and downstream velocity (Scavia et al., 2013). The summer HA is determined by hypoxic length (HA=57.8 hypoxic length)
59 derived from summer bottom DO concentration. The model explains 69 % of the variability in observed HA by the mid-
60 summer Shelf-wide cruises. Mechanistic prediction methods have also been applied by Laurent and Fennel (2019) to develop
61 a weighted mean forecast that is calibrated using May nitrate loads and three-dimensional hindcast simulations over the period
62 1985–2018. Once calibrated, the model only requires May nitrate loads as an input to produce the seasonal forecast for a given
63 year. The model can explain up to 76 % of the year-to-year variability of the HA observation. However, the model is not
64 favorable for years with strong wind events during summer.

65 These above-mentioned models share some similar drawbacks. (1) The effects of water column stratification are considered
66 only implicitly by the associated wind speeds, water transport, and riverine nutrient loads (usually correlated to river
67 discharges), although stratification is documented as a crucial factor in regulating HA variability. (2) Forecast of the predictors
68 is usually limited, which restricts some of these seasonal models to pseudo ones. (3) Most models are only capable of capturing
69 interannual HA variability and are not reliable in summers when winds are strong. According to the hindcast results by our
70 three-dimensional coupled hydrodynamic–biogeochemical model described in the accompanying paper (Part I), strong wind
71 events bring considerable uncertainties to monthly and daily variabilities of HA. In this study we aim to provide a novel HA
72 prediction method that considers both stratification and biochemical effects. Our new model aims to produce daily HA
73 forecasts based on selected predictors' forecasts with a minimum computational cost. The rest of the paper is organized as
74 follows. Detailed descriptions of methods and data are given in section 2. The employments of generalized linear models
75 (GLMs), generalized additive models (GAMs), and an independent model application using a global forecast product (HYbrid
76 Coordinate Ocean Model, HYCOM; Bleck and Boudra, 1981; Bleck, 2002) are given in section 3. Comparisons against
77 existing forecast models, recommendations on nutrient reduction strategy, and model improvement outlook are given in section
78 4.

79 **2 Methods**

80 **2.1 Data preparation**

81 We adapted a three-dimensional coupled hydrodynamic–biogeochemical model embedded in the framework of the Regional
82 Ocean Modeling System (ROMS) on the platform of Coupled Ocean–Atmosphere–Wave–Sediment Transport Modelling
83 system (COAWST, Warner et al., 2010) to the GoM (Gulf–COAWST, for detailed descriptions, validations, and results of the
84 numerical model see Part I). Numerical hindcasts (hereafter denoted as ROMS hindcasts or ROMS simulations) are output
85 daily from 1 January 2007 to 26 August 2020 and spatially averaged over the LaTex Shelf extending from the west of
86 Mississippi River mouth to 95°W with water depths ranging from 6 to 50 m (color shaded region in Figure A1b).

87 **2.1.1 Hydrodynamic-related predictors**

88 Both water stratification and bottom biochemical processes modulate the variability of bottom DO concentration in the LaTex
89 Shelf. Potential energy anomaly (PEA, in J m^{-3}) is introduced as an estimate of water column stratification according to:

90

91 $$PEA = \frac{1}{H}\int_{-h}^{\eta}(\bar{\rho} - \rho)gzdz, \tag{1}$$

92

93 where ρ is water density profile (estimated by water temperature and salinity profiles) over water column of depth $H = h + \eta$,
94 h is the location of the bed, η is water surface elevation, g is the gravitational acceleration (9.8 m s^{-2}), z is the vertical axis, $\bar{\rho}$

95   is the depth-integrated water density given by $\bar{\rho} = \frac{1}{H} \int_{-h}^{\eta} \rho \, dz$ (Simpson and Hunter, 1974; Simpson et al., 1978; Simpson,

96   1981; Simpson and Bowers, 1981). The PEA represents the amount of energy per volume required to homogenize the entire

97   water column (Simpson and Hunter, 1974). Thus, a greater PEA value represents a more stratified water column. As a river-

98   dominated area, water stratification in the LaTex Shelf is highly affected by freshwater-induced buoyancy from the Mississippi

99   and Atchafalaya Rivers. Sea surface salinity (SSS) is a good proxy for representing the distribution and variability of river

100   freshwater across the shelf. Indeed, the correlation of regionally averaged PEA and SSS is significantly high as -0.87 ($p < 0.001$;

101   Figure 1a) which emphasizes the importance of freshwater-induced stratification. Therefore, we considered SSS as another

102   candidate predictor besides PEA.

103

104   Surface heating and wind mixing are two other factors that influence water stratification (Simpson, 1981). The tidal effects

105   considered in Simpson (1981) are neglected here due to the relatively weaker contribution in stratification in the shelf when

106   compared to the effects of rivers and winds. The two mixing terms are quantified as follows:

107

108   $\frac{d(PEA)}{dt} = \frac{\alpha g}{2c} Q - \delta k_a \rho_a W^3,$ (2)

109

110   where Q is the rate of surface heat input, α is the volume expansion coefficient, c is water specific heat capacity, δ is a

111   coefficient of wind mixing, k_a is drag coefficient, ρ_a is humid air density near the sea surface, and W is the wind speed near

112   the sea surface. The first term on the right-hand side of Eq. (2) represents the rate of change of water stratification due to

113   surface heating, while the second term is the rate of working by wind stress contributing negatively to water stratification.

114   Therefore, the heat-induced change of PEA is proportional to surface heat input, which is,

115

116   $d(PEA)_{heat} \propto Q,$ (3)

117

118   The total net heat flux, a sum of net shortwave and net longwave radiation flux, is derived from the National Centers for

119   Environmental Prediction Climate Forecast System (NCEP) Reanalysis (CFSR) 6-hourly products (Saha et al., 2010; 2011) in

120   this study. The term Q is added to the candidate list of predictors and is denoted as PEA_{heat} (heat-induced PEA changes) for

121   simplification (Figure 1a).

122

123   Daily variability of term ($\delta k_a \rho_a W^3$) is dominated by that of W^3, since the ρ_a fluctuates much less than the W^3 on a daily

124   scale (Figure A2). We obtained the ρ_a according to (Picard et al., 2008) :

125

126   $\rho_a = \frac{pM_d}{ZRT} \left[1 - x_v \left(1 - \frac{M_v}{M_d} \right) \right],$ (4)

127

128   where p represents the absolute air pressure, M_d (=28.96546 g mol^{-1}) is the molar mass of dry air, M_v (=18.01528 g mol^{-1}) is

129   the molar mass of water vapor, Z indicates compressibility, R (=8.314472 J mol^{-1} K^{-1}) is the molar gas constant, T is

130   thermodynamic temperature, x_v is the mole fraction of water vapor. We assumed that air parcels at the sea surface are ideal

131   gases ($Z = 1$) and are always saturated with water vapor. Thus, x_v is a function of absolute air pressure (p) and saturation

132   vapor pressure of water (p_{sat}) and can be calculated as follows:

133

134    $$x_v = \frac{p_{sat}}{p}, \tag{5}$$

135

136   According to the adjusted Tetens equation (Murray, 1967; Monteith and Unsworth, 2014), p_{sat} (in Pa) can be estimated by:

137

138    $$p_{sat} = 611 e^{\frac{17.27(T-237.3)}{T-T'}}, \tag{6}$$

139

140   where $T' = 36$ K. Substitute Eqs. (5)–(6) to Eq. (4) with the assumption of $Z = 1$, we obtained air density as a function of both

141   air pressure and air temperature in the following:

142

143    $$\rho_a = \rho_a(T,p) = \frac{pM_d}{RT}\left[1 - \frac{611}{p}\left(1 - \frac{M_v}{M_d}\right)e^{\frac{17.27(T-237.3)}{T-T'}}\right], \tag{7}$$

144

145   The ρ_a is then estimated using sea surface air pressure and air temperature 2 meters above the sea surface provided by NCEP

146   CFSR 6-hourly products. The correlation of daily $\rho_a W^3$ and W^3 (provided by NCEP CFSR 6-hourly products) is significantly

147   high as 0.9988 ($p<0.001$, Figure A2) emphasizing the importance of term W^3 in controlling the daily variability of wind-

148   induced PEA changes over the shelf. We, thus, approximated the relationship as:

149

150    $$d(PEA)_{wind} \propto W^3, \tag{8}$$

151

152   The term W^3 is introduced as another candidate predictor and is denoted as PEA$_{wind}$ (wind-induced PEA changes) for

153   simplification (Figure 1a).

154   **2.1.2 Biochemical-related predictors**

155   Sedimentary biochemical processes directly influence the bottom DO consumption rate. However, global forecast models such

156   as HYCOM do not cover biochemical parameters. Therefore, the biochemical-related term SOC needs to be replaced by an

157   alternative term (denoted as SOCalt). According to the SOC scheme (Eq. 9) stated in Part I, the biochemical features are

158   attributed to the sedimentary particulate organic nitrogen concentration (PONsed, derived from ROMS hindcasts). The total

159 nitrate+nitrite loads by the Mississippi River are used to represent the PONsed variability due to the long-term data supports.

160 The daily Mississippi River discharges at site 07374000 are updated daily by the U.S. Geological Survey (USGS) National

161 Water Information System (NWIS) since March 2004. The total nitrogen concentration at site 07374000 is provided and

162 updated daily by USGS since November 2011. Prior to 2011, nitrogen loads (at site 07374000) are provided monthly by USGS

163 and, in this study, are interpolated to daily intervals according to the corresponding monthly loads. Although phosphate and

164 silicate are another two limitation nutrients in the shelf, daily measurement are still not available for the Mississippi River.

165 Monthly total nitrate+nitrite loads, phosphate loads, and silicate loads by both the Mississippi River and the Atchafalaya River

166 are significantly correlated (Table A1). Therefore, the total nitrate+nitrite loads applied here can be interpreted as total nutrient

167 loads by both river systems. Due to lateral transports and vertical settling of particulate organic matter, a leading period should

168 be introduced to the time series of riverine nutrient loads. The optimal length of leading days is obtained by examining the

169 highest linear correlation of regionally averaged ROMS-hindcast SOC and SOCalt (Eq. (10)) and is calculated as 44 days

170 (R=0.7427, p<0.001, Figure A3a). The exponential term in Eqs. (9)–(10) estimates the temperature-dependent decomposition

171 rate of organic matter.

172 $SOC = PON_{sed} \cdot VP2N_0 \cdot e^{K_{P2N} \cdot T_b}$,   (9)

173 $SOCalt =$ Mississippi River inorganic nitrogen loads (led by 44 days) $\cdot e^{0.0693 T_b}$,   (10)

174

175 $VP2N_0$ is a constant representing the decomposition rates of sedimentary particulate organic nitrogen, PON_{sed}, at 0 ºC. K_{P2N}

176 is a constant (0.0693 ºC^{-1}) indicating temperature coefficients for decomposition of PON_{sed}. T_b is bottom water temperature

177 (in ºC). The Q10 (= 2 given the above chosen coefficients; van't Hoff and Lehfeldt, 1899; Reyes et al., 2008) assumption is

178 applied to mimic the aerobic decomposition rate of PON_{sed}. Along with SOCalt, the temperature-dependent decomposition

179 rate $e^{0.0693 \cdot T_b}$ is also considered as a candidate predictor in statistical models and is denoted as DCP$_{Temp}$ for simplification.

2.1.3 HA estimation

181 As listed in Table 1, six candidate predictors are considered in the statistical models including four stratification-related

182 variables (PEA, SSS, PEA$_{heat}$, and PEA$_{wind}$) and two bottom biochemical variables (SOCalt and DCP$_{Temp}$). The correlation

183 coefficient matrix (Figure 1a) indicates that multicollinearity may become a problem in regression models since linear

184 correlations among some predictors are significantly high, e.g., 0.74 (p<0.001) between PEA and SOCalt, and -0.87 (p<0.001)

185 between PEA and SSS. The multicollinearity can harm the assumption that predictors are independent. It can lead to difficulties

186 in individual coefficients test and numerical instability (Siegel and Wagner, 2022). The frequency distribution of HA (Figure

187 1b) illustrates that the response variable is highly right-skewed with ~42 % of samples (2,081 out of 4,943) being exactly zero.

188 The HA is estimated by the number of hypoxia cells (ROMS computational cells reaching hypoxic conditions) times a nearly

189 constant value (area of the computational cell), which is 25.56 $\pm$ 0.17 km^2 (mean $\pm$ 1SD). Thus, the HA can be estimated by

190 the number of grid cells when the Poisson and negative binomial regression models are applied. However, the great portion of

191 zero samples leads to overdispersion (magnitude of variance $\gg$ magnitude of mean, i.e., 45,730,441 $\gg$ 4,507) and zero-

192   inflated problems (Lambert, 1992). The overdispersion issue violates the mean-variance equality assumption employed in

193   regular Poisson regression models, while zero-inflated problems can weaken the model performances.

194   **Table 1. Description of daily response variable and candidate predictors. The data cover a time range from 1 January**
195   **2007 to 26 August 2020. Prescribed min and max are used for min-max normalization.**

| Variables [units]	Description	Min	Median	Mean	Max	Prescribed (Min:Max)
HA [km^2]	Hypoxic area (when bottom dissolved oxygen < 2 mg L^{-1})	0	1,137	4,507	34,097	Non-normalized
PEA [J m^{-3}]	Potential energy anomaly measuring the water stratification	3.3	35.6	47.2	187.9	(0:200)
SSS [non-dim]	Sea surface salinity	20.0	30.8	30.4	33.9	(0:40)
PEA$_{heat}$ [W m^{-3}]	=Q, an approximation of surface heat-induced water stratification	-54.4	151.9	142.7	261.3	(-60:300)
PEA$_{wind}$ [m^3 s^{-3}]	=W^3, an approximation of water stratification changes due to wind mixing	0.5	164.7	296.1	7013.2	(0:7,100)
SOCalt [mmol s^{-1}]	An alternative term for sediment oxygen consumption.	789,319	10,423,383	13,377,287	41,984,069	(770,000:43,000,000)
DCP$_{Temp}$ [non-dim]	$= e^{0.0693 \cdot T_b}$, temperature-dependent decomposition rate of organic matter	2.6	5.1	5.2	8.0	(0:10)

196

2.2 Data pre-processes

198   We first spatially averaged ROMS-derived predictors (daily) over the LaTex Shelf (color-shaded area in Figure A1b), then

199   applied the min-max normalization (Eq. (11)) to the one-dimensional time series. Predictive models can be beneficial from the

200   min-max normalization when applying to a new dataset since the method guarantees that the normalized predictors from

201   different datasets range from 0 to 1 as the minimum and maximum values are prescribed. Note that the response is not

202   normalized.

203

204 $$X_{nor} = \frac{X_{org} - Min_{prescribed}}{(Max_{prescribed} - Min_{prescribed})},$$ (11)

205

206 where X_{nor}, X_{org}, $Min_{prescribed}$, and $Max_{prescribed}$ represent normalized value, original value, prescribed minimum, and

207 prescribed maximum, respectively. The daily samples are then split into a training set (for model construction) accounting for

208 80 % of the total samples and a test set (for assessment of model performances) accounting for the remaining 20 %. To maintain

209 the HA distribution in both sets, a random resampling method is applied in different HA intervals individually. For example,

210 80 % of samples with HA=0 are chosen randomly for the training set out of all daily samples with HA=0, while the rest of the

211 samples with HA=0 are grouped into the test set. The HA=0 is the first interval to which the resampling process is applied,

212 while the remaining samples are split at intervals of 5,000 km². However, the distribution of HA from each year is similar with

213 a right-skewed structure and numerous zero values. Thus, even through random processes, both the training and test sets

214 contain samples from each year including samples with non-peak and peak HA. This splitting method increases the model

215 applicability and provides a comprehensive assessment of prediction performances on both non-peak and peak HA.
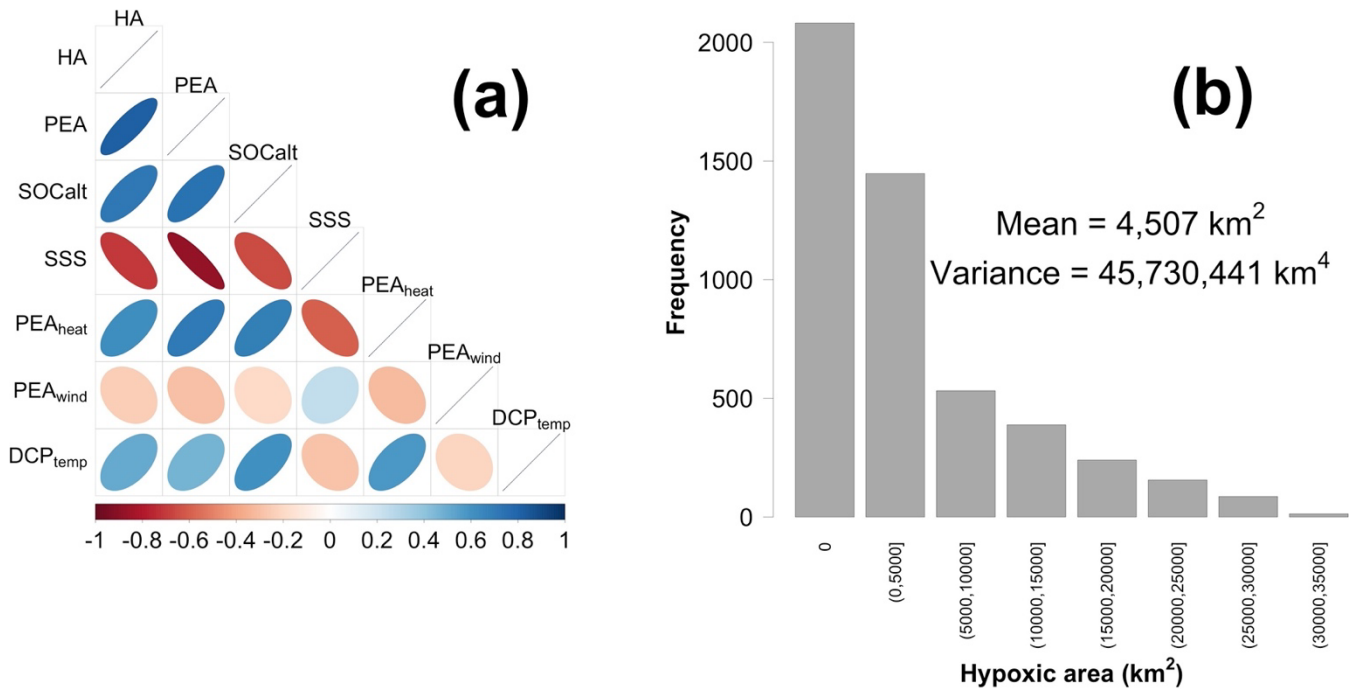
216

217 **Figure 1. (a) A correlation coefficient matrix of the response variable and candidate predictors, and (b) the frequency distribution**
218 **of HA. Data are provided daily from 1 January 2007 to 26 August 2020.**

219 **2.3 Model skill assessment**

220 The R^2, root-mean-square error (RMSE), mean absolute percentage bias (MAPB), and scatter index (SI; Zambresky, 1989)

221 are used to assess the model performances in HA predictions. The SI is a normalized measure of error or a relative percentage

222 of expected error with respect to the mean observation. The calculations of the statistics are given in Eqs. (12) – (15).

8

223 $R^2 = 1 - \frac{\sum_{i=1}^{N}(P_i - O_i)^2}{\sum_{i=1}^{N}(P_i - \bar{O})^2}$ (12)

224

225 $RMSE = \sqrt{\frac{\sum_{i=1}^{N}(P_i - O_i)^2}{N}}$ (13)

226

227 $MAPB = \frac{1}{N}\sum_{i=1}^{N}\left|\frac{P_i - O_i}{O_i}\right| \times 100\%$ (14)

228

229 $SI = \frac{RMSE}{\bar{O}} \times 100\%$ (15)

230 where P_i and O_i represent the ith record of prediction and observation (or hindcast), while $\bar{O}$ represents the average of all

231 observed (or hindcast) records.

232 **3 Model construction and results**

233 **3.1 Model built-up process**

234 Several regression models are explored using the statistical programming language R. To find the "best" model balancing both

235 model interpretability and prediction performance, a procedure is conducted for model selection (Figure 2) and is summarized

236 below. (1) Choose a regression model. (2) Apply an exhaustive best-subset searching approach to the chosen model. Models

237 with possible combinations of candidate predictors from the ROMS training set are built. A 10-fold cross-validation (CV)

238 method is applied to each model yielding 10 RMSEs and 1 corresponding mean. The candidate predictors of PEA and SOCalt

239 are forced into each subset. Thus, the number of fitted models with a subset size of k is $C(6 - 2, k - 2) = \frac{4!}{(6-k)!(k-2)!}, 2 \leq$

240 $k \leq 6$ (the total number of candidate predictors is 6). The optimal subset of this size is found as the one with the lowest mean

241 CV RMSE among these models. The best subset is then obtained by comparing mean CV RMSEs of the optimal subsets of

242 different sizes. (3) Steps (1)–(2) are repeated for the selected M candidate regression models. (4) Prediction performances of

243 different models with the corresponding best subsets are assessed by the 10-fold CV RMSEs and Bootstrap (1,000 iterations)

244 aggregating (i.e., Bagging) ensemble algorithms. The Bagging method builds the given model N (=1,000) times during each

245 of which the given model is trained using different samples chosen randomly and repeatedly from the ROMS training set and

246 is executed for HA prediction using samples in the ROMS test set. The ensemble means and ensemble 95 % prediction intervals

247 (PIs) of forecast HA are given according to the prediction results in the 1,000 iterations. The best model (Model X in Figure

248 2) is chosen according to the comparisons of the 10-fold CV RMSEs and the Bagging results.
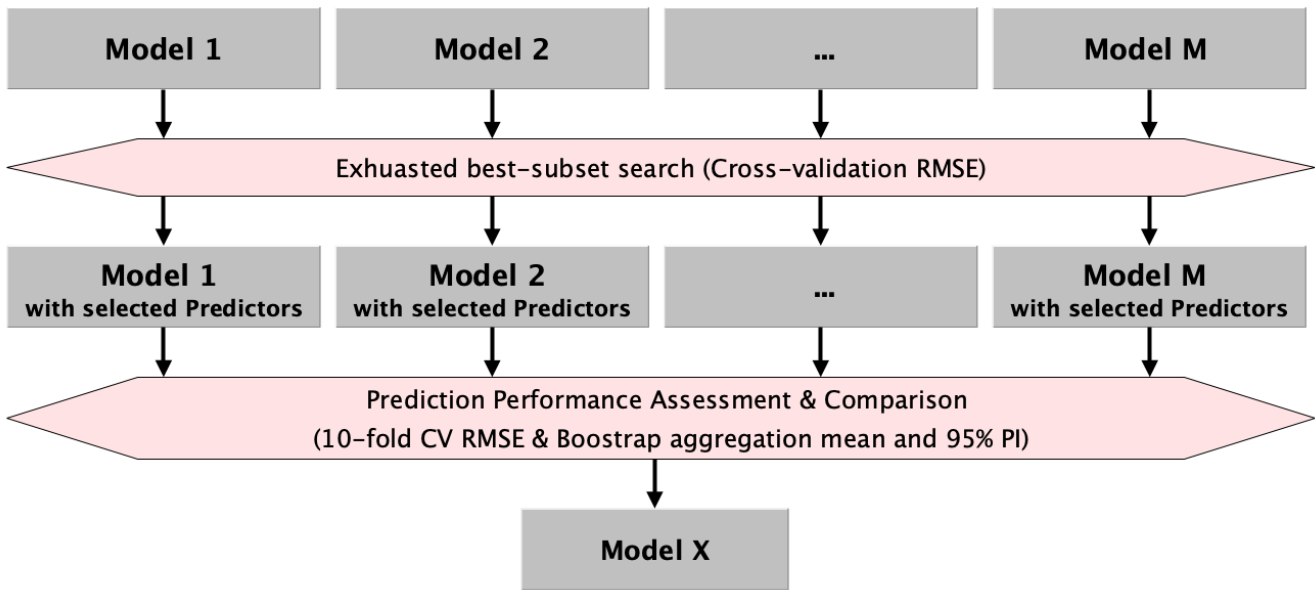
249

250

Figure 2. A flow chart of building up regression models.

3.2 Generalized linear models (GLMs)

3.2.1 Regular GLMs and zero-inflated GLMs

The response variable can be treated as count data. Regular Poisson (function glm in R package "stats" version 3.6.2), quasi-Poisson (function glm in R package "stats" version 3.6.2), and negative binomial (function glm.nb in R package "MASS" version 7.3-54; Venables and Ripley, 2002) GLMs are explored in this section. The latter two GLMs are known for solving overdispersion problems by relaxing the mean-variance equality assumption. These GLMs make use of a natural log link function. Thus, a natural logarithm of the area of a single ROMS cell (~ 25.56 km^2) is added to the models as an offset term (an additional intercept term).

In addition, the overdispersion issue can result from the great percentage ($\sim$42 %) of zero values in the response variable (Figure 1b). Zero-inflated GLMs (using function zeroinfl in R package "pscl" version 1.5.5; Jackman, 2020; Zeileis et al., 2008) are developed for dealing with response variables of this kind. Rather than resetting dispersion parameters, a zero-inflated count model is a two-component mixture model blending a count model and a zero-excess model. The count model is usually a Poisson or negative binomial GLM (with log link), while the zero-excess model is a binomial GLM (with logit link in this study) estimating the probability of zero inflation. An offset term of log (25.56) is also introduced into the count model. Instead of applying the best-subset searching to the count and zero-excess models simultaneously, in this study, the searching is conducted respectively for these two models to reduce the demands of computational resources. The best subset of the zero-

269 excess model (binomial GLM) is given first. The best subset of the count model (Poisson or negative binomial GLMs) is then

270 provided blending the zero-excess model with the corresponding selected best subset fixed.

271

272 However, it is hard to determine whether a given zero value of HA is excessive, instead, it is relatively easy to model hypoxia

273 occurrence assuming that all the zero values are excessive. A new binary response, hypoxia, stated in Eq. (16) is introduced

274 for modeling hypoxia occurrence using regular binomial GLMs (function glm in R package "stats" version 3.6.2). The hypoxia

275 is equal to 0 when HA is 0 (no hypoxia), otherwise, is equal to 1. The optimal model selected three predictors: PEA, SOCalt,

276 and DCP_{Temp} (Figure 3b).

277

278 $hypoxia = \begin{cases} 0, & no\ hypoxia \\ 1, & hypoxia\ occurs \end{cases}$, (16)

279

280 **3.2.2 Performance of GLMs**

281 The zero-inflated Poisson GLM serves as the best GLM in terms of prediction performances since it has the lowest mean CV

282 RMSE (Figure 3a) among the five candidates GLMs. The relaxation of the mean-variance equality assumption by the negative

283 binomial GLM and the quasi-Poisson GLM does not guarantee salient improvement of performances when comparing their

284 CV RMSEs to those of regular Poisson GLM. The zero-inflated negative binomial GLM yields similar performances to the

285 three regular GLMs. The mean CV RMSEs of zero-inflated Poisson GLM hit the trough (3,573 km^2) at the size of four.

286 However, the greatest drop of RMSEs (3,586 km^2) occurs at the size of three beyond which the RMSEs remain stable. It is

287 worth considering a model with fewer predictors satisfying model interpretability. Thus, the best zero-inflated Poisson GLM

288 accounts for three predictors (PEA, SOCalt, and DCP_{Temp}) in the count model and three predictors (PEA, SOCalt, and DCP_{Temp})

289 in the zero-excess model. As indicated in the correlation matrix (Figure 1a), the robustness of a model can be impaired by

290 multicollinearity which can be estimated by variance inflation factors (VIFs). VIFs among the selected predictors are 2.15,

291 2.70, and 1.59 for PEA, SOCalt, and DCP_{Temp}, respectively. The VIFs are all less than 5 suggesting that both the count and the

292 zero-excess models with these predictors involved are merely violated by multicollinearity. For simplicity, the best zero-

293 inflated Poisson GLM is symbolized as GLMzip3.

294

295 The Bagging ensemble method is implemented to estimate the prediction performance of GLMzip3 (Figure 4a). It is noted

296 that the training set and test set are resampled according to different HA intervals. Since the distributions of HA in each year

297 are similar (see Section 2.2), HA in both training and test set contains observations of peak and non-peak values in each year.

298 Therefore, samples shown in Figure 4 are listed sequentially in the time dimension from 2007 to 2020 but are not necessarily

299 evenly distributed. The listed samples should not be regarded as time series. The Bagging means of predicted HA provides an

300 RMSE of 3,614 km^2 and an R^2 of 0.7214 against the ROMS hindcasts. The Bagging 95 % PIs are restricted within a narrow

301 range with a slight increase at the predicted peaks. Within different ranges of hindcast HA, the MAPB between predicted and

302 hindcast HA ranges from 29 % to 38 % with an average of 33 % (Table 2). Particularly, the GLMzip3 produces the lowest

303 bias (29 %) for the hindcast HA $\geq$ 30,000 km^2. The results suggest that GLMzip3 is capable of providing not only accurate

304 but also stable HA forecasts. Nevertheless, we noted salient overestimations (e.g., peaks around samples 30, 481, and 901) and

305 underestimations (e.g., peaks around samples 181, 390, and 826) at some peaks. Instead of the prediction performance at non-

306 peak HA, here we focused more on the forecasts at HA peaks which impose more threats to the shelf ecosystem. In section

307 3.3, GAMs are investigated with an expectation of further improvements in peak predictions by considering non-parametric

308 or non-linear effects of the predictors.
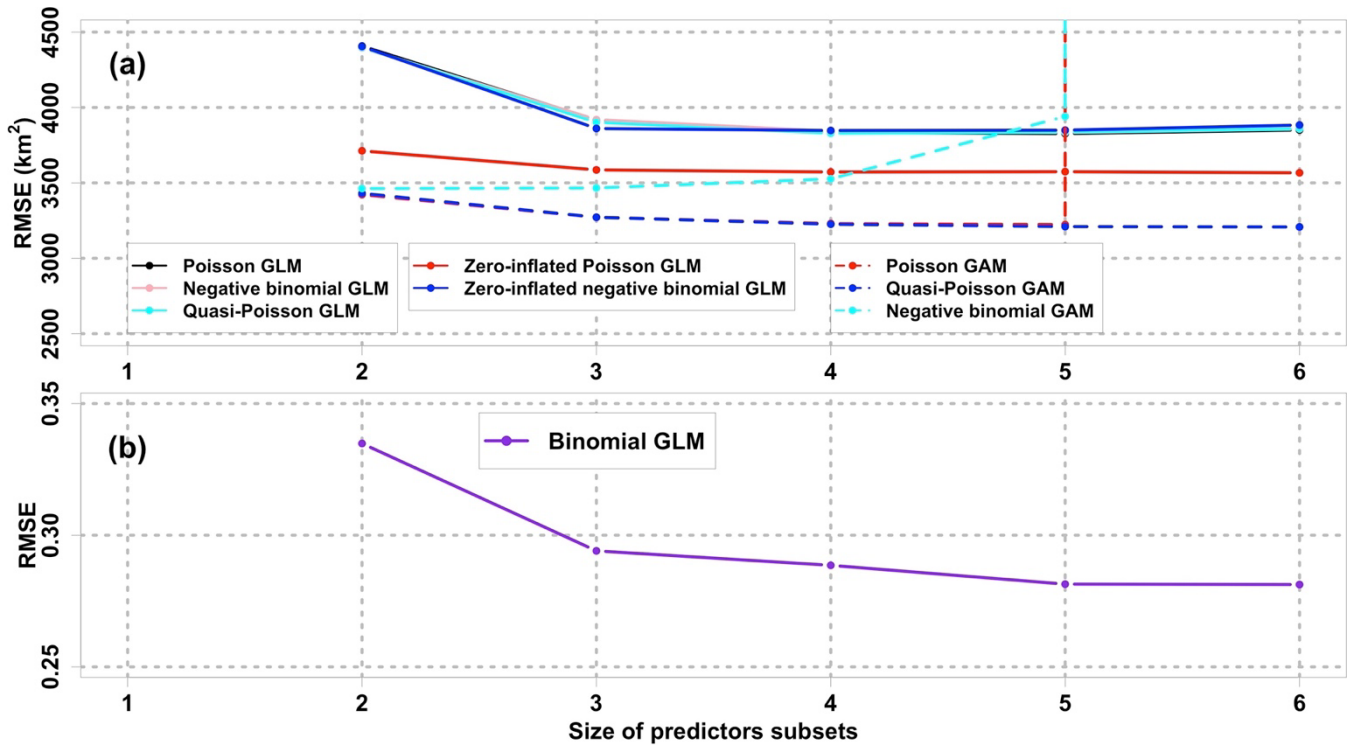
309
310 **Figure 3. Comparisons of mean 10-fold CV RMSEs among different regression models with various sizes of predictors subsets. The**
311 **response variable in (b) binomial GLM and (a) other models is hypoxia occurrence (hypoxia) and hypoxic area (HA), respectively.**
312 **Note that the CV RMSEs of negative binomial GAM and Poisson GAM with the size of six are out of the range shown. CV RMSE**
313 **curves of the Poisson GLM, negative binomial GLM, and quasi-Poisson GLM overlap, while those of Poisson GAM and quasi-**
314 **Poisson GAM overlap when size $\leq$ 5. The minimum size of predictor subsets is two since PEA and SOCalt are forced into every**
315 **subset.**

12
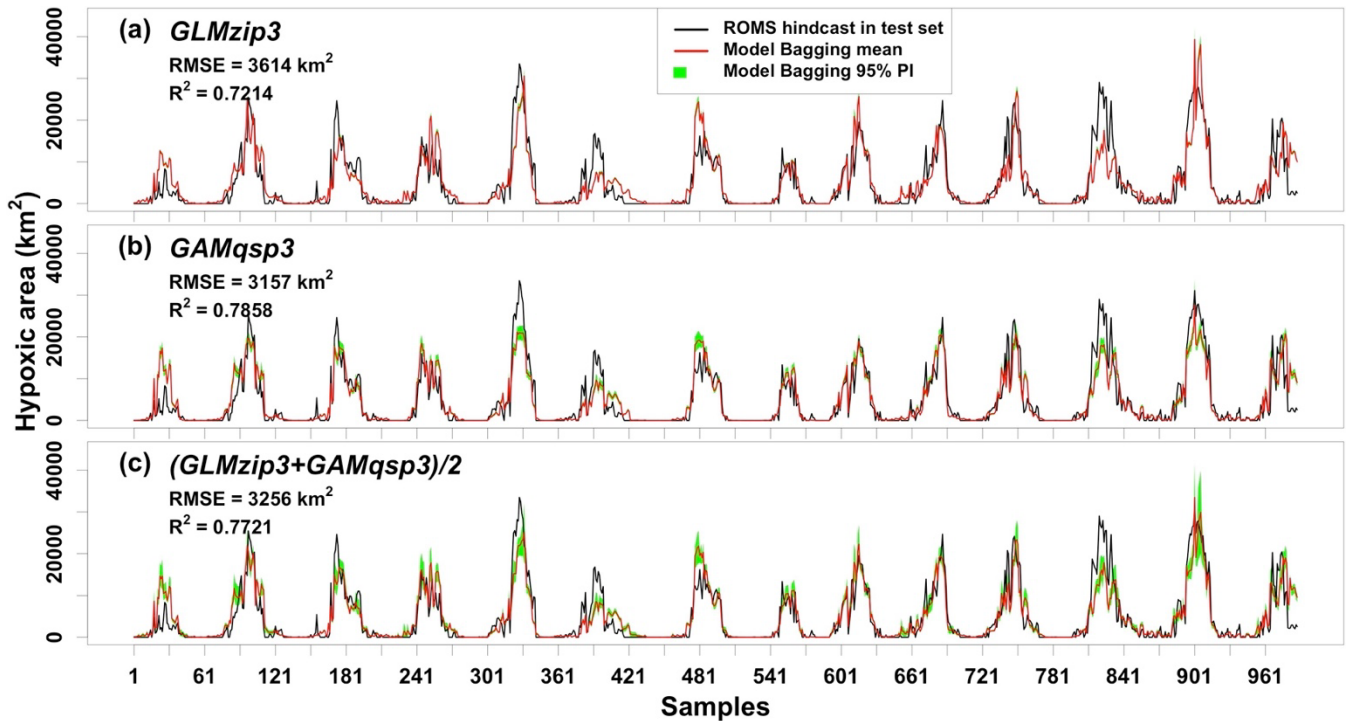
316
317 **Figure 4. Comparisons of model predicted HA and ROMS-hindcast HA in the test set. RMSEs and R²s are derived between model**
318 **Bagging mean and ROMS-hindcast HA.**

319 **Table 2 Mean absolute percentage bias between predicted and hindcast HA in the test set within different ranges of hindcast HA.**
320 **The mean bias when hindcast HA $<$ 5,000 km² is not shown since the prediction accuracy at high HA ranges is a more important**
321 **feature of HA prediction models. The threshold of 5,000 km² is chosen because it is the goal HA set by the Action Plan (Mississippi**
322 **River/Gulf of Mexico Watershed Nutrient Task Force, 2001; 2008). HA above this threshold is more worthy of attention.**

Hindcast HA range (km²)	GLMzip3	GAMqsp3	Ensemble
[5000, 10000]	38	40	36
[10000, 20000]	32	25	28
[20000, 30000]	34	26	28
$\geq$ 30000	29	28	25
Average	33	30	29

323

324 ### 3.2.3 Model interpretation for GLMzip3

325 We applied the complete ROMS training set to the model construction of GLMzip3. Coefficients for PEA, SOCalt, and
326 DCP$_{Temp}$ (Table 3) are all found significantly positive ($p<0.001$) in the count model, while coefficients for these predictors are
327 significantly negative ($p<0.001$) in the zero-excess model. The count model simulates the HA while the zero-excess model
328 estimates the probability of HA being zero. Higher PEA is consistent with stronger water stratification, while higher SOCalt

13

329 and DCP$_{Temp}$ are both corresponding to higher sediment oxygen consumption. Therefore, there is no surprise that higher PEA,
330 SOCalt, and DCO$_{Temp}$ are related to greater HA and higher hypoxia occurrence or lower probability of HA being zero. Results
331 indicate that the GLMzip3 essentially builds up reasonable relationships between the response and predictors variables with a
332 high agreement with physical and biochemical mechanisms. Since the ranges of normalized predictors are from 0 to1,
333 comparisons of regression coefficients indicate that effects of PEA (2.8037 in the count model and -10.4439 in the zero-excess
334 model, same hereafter) are considered more important than SOCalt (0.9057 and -7.3100) and DCP$_{Temp}$ (0.8425 and -95698).
335 The result is consistent with the findings of previous studies which emphasized that the physical impacts are stronger than the
336 biological impacts on HA estimates (Yu et al., 2015; Mattern et al., 2013).

337 **Table 3. Regression coefficients of GLMzip3.**

Count model coefficients (Poisson with log link):				Zero-excess model coefficients (binomial with logit link):			
	Estimate	Std. Error	z value	Pr (> |z|)		Estimate	Std. Error	z value	Pr (> |z|)
Intercept	3.6397	0.0017	2120.5	<2E-16***	Intercept	7.7641	0.2761	28.12	<2E-16***
PEA	2.8037	0.0014	1984.6	<2E-16***	PEA	-10.4439	0.6794	-15.37	<2E-16***
SOCalt	0.9057	0.0014	639.6	<2E-16***	SOCalt	-7.3100	0.5714	-12.79	<2E-16***
DCP$_{Temp}$	0.8425	0.0029	287.7	<2E-16***	DCP$_{Temp}$	-9.5698	0.4611	-20.75	<2E-16***

Significance codes: 0 (***)   0.001 (**)   0.01 (*)

Log-likelihood: -2.675E6 on 8 degrees of freedom

3.3 Generalized additive models (GAMs) and the ensemble model

340 GAMs are explored with an expectation of improving prediction performance in HA peaks by introducing non-parametric
341 effects of predictors. Using function "gam" in R package "mgcv" (version 1.8-36; Wood, 2011) with smooth functions as pure
342 thin plate regression splines (degree of freedom=9; Wood, 2003), three GAMs are studied and compared, i.e., Poisson GAM,
343 quasi-Poisson GAM, and negative binomial GAM. Following the same procedure in GLM exploration, the best subset
344 searching approach is applied to the GAMs first. Although mean 10-fold CV RMSEs for the Poisson and quasi-Poisson GAMs
345 (Figure 3a) exhibit insignificant differences at sizes from two to five, the CV RMSEs for the former increase dramatically at a
346 size of six, which indicates that the model stability decreases with sizes. The negative binomial GAM has the greatest mean
347 CV RMSEs among the GAMs studied and has an extremely high mean CV RMSE at the size of six. The quasi-Poisson GAM
348 is considered the best GAM among the three. Although the mean CV RMSEs for the quasi-Poisson GAM reach the lowest at
349 the size of six, the best size is considered as three (including PEA, SOCalt, and DCP$_{Temp}$) at which CV RMSEs exhibit the
350 most saline decline, and beyond which mean CV RMSEs stabilize around 3,200 km^2. The quasi-Poisson GAM with three
351 predictors involved is symbolized as GAMqsp3.
352

353 Component plots of the GAMqsp3 (Figure 5) imply that HA generally increases as the chosen predictors increase. Note that
354 the summation of all smooth function terms contributes directly to the log of fitted HA. Such results agree with those found
355 by model GLMzip3. However, the component plots provide more detailed information about the rate of changes in HA. The
356 effective degrees of freedom range from 6.79 to 8.90 indicating strong non-linear effects of the predictors on the variability of
357 HA. The HA is more sensitive to the predictors in the low-value ranges but becomes nearly stable in the medium- and high-
358 value ranges of predictors. This implies that bottom hypoxia develops rapidly in early summer when water stratification and
359 sediment oxygen demand start to increase. On the other hand, the smooth functions of SOCalt and DCP_{Temp} have a sharper
360 slope than that of PEA at the low-value range. It suggests that at the first stage of hypoxia development in late spring and early
361 summer, sedimentary biochemical processes contribute more than water stratification. The bottom hypoxic water further
362 extends with a much lower expansion speed as the stratification and SOCalt further intensify. Nevertheless, the smooth function
363 of PEA is slightly greater also with a more acute slope than those found for SOCalt and DCP_{Temp} in the medium- and high-
364 value regimes of the predictors. It indicates that the HA variability is more related to the hydrodynamic changes in the shelf
365 than the biochemical effects during mid-summers. The result is consistent with the findings by Yu et al., (2015) and Mattern
366 et al. (2013). The GAMqsp3 model provides reasonable interpretations on the hypoxic area mechanisms.
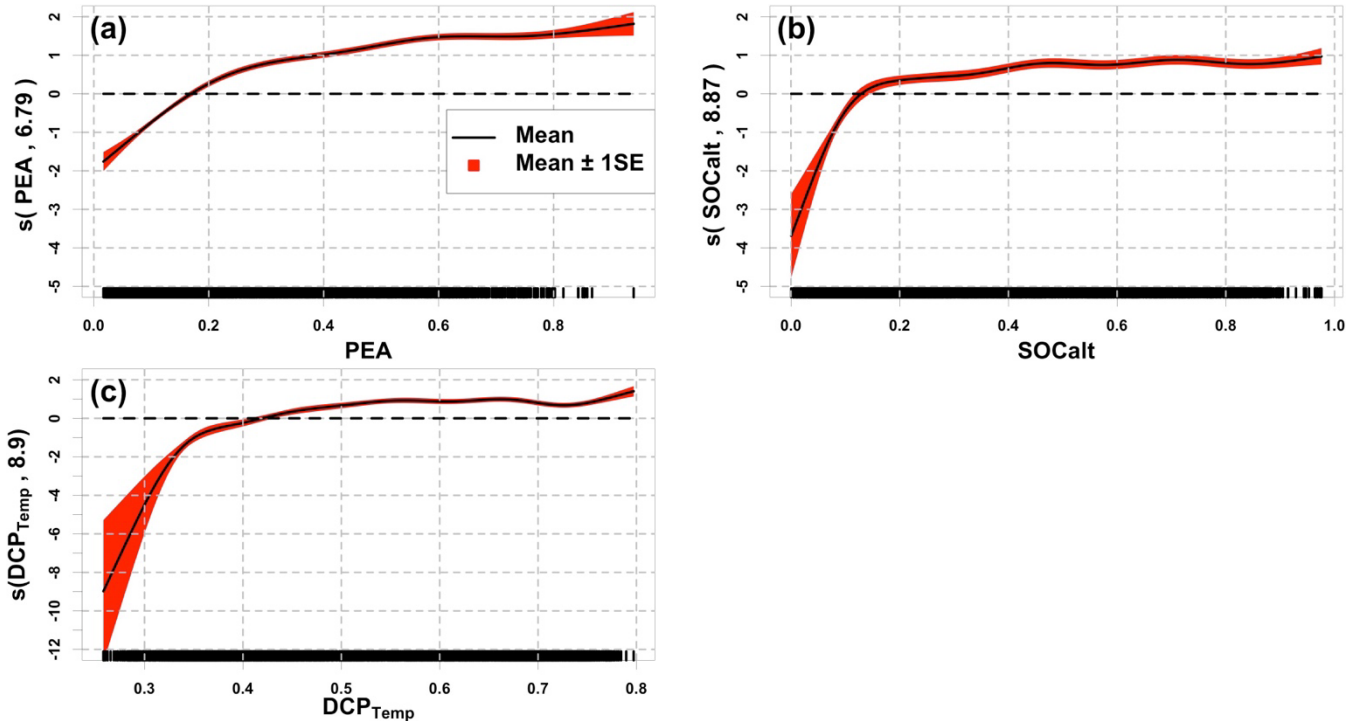
367
368 **Figure 5. Component plots of model GAMqsp3. Solid black lines represent the mean of the smooth function, while the red area**
369 **denotes the range of mean ± 1SE. Numbers in brackets represent effective degrees of freedom for the corresponding smooth terms.**
370 **Black bars at the x axis indicate the density of corresponding normalized predictors. Dashed black lines are straight lines of zero**
371 **along the predictor domains.**

372   The prediction performance of GAMqsp3 is estimated using the Bagging ensemble method (Figure 4b). The RMSE and R^2

373   between the Bagging mean and ROMS-hindcast HA is 3,157 km^2 and 0.7858, respectively. They are 13 % lower and 9 %

374   higher than the corresponding statistics found for the GLMzip3, respectively. MAPB between GAMqsp3 predicted and

375   hindcast HA ranges from 25 % to 40 % with an average of 30 % (Table 2). Such statistics are generally lower than those found

376   in GLMzip3. Results suggest that GAMqsp3 outcompetes GLMzip3 in terms of overall performance. However, GAMqsp3

377   tends to underestimate HA peaks (like those seen at peaks around samples 750 and 901) some of which are overestimated by

378   the GLMzip3. Therefore, instead of determining the best model out of the two, ensemble HA predictions blending efforts of

379   both GLMzip3 and GAMqsp3 are carried out with an expectation to improve model performance in the peak forecast. We

380   assumed that the contributions of GLMzip3 and GAMqsp3 are equally weighted and thus averaged the predicted HA by

381   GLMzip3 and GAMqsp3 and calculated the 95 % PIs given the Bagging results of these models (Figure 4c). As expected, the

382   overall performance of the ensemble forecast is somewhere between the performance of GLMzip3 and GAMqsp3 with an

383   RMSE of 3,256 km^2 and an R^2 of 0.7721. However, some HA peak events (like peaks around samples 750 and 901) which are

384   overestimated by GLMzip3 but are underestimated by GAMqsp3 are accurately predicted by the ensemble approach. MAPB

385   also indicates an increase in peak prediction performance by the ensemble model. The statistic is within a range of 25 % to 36

386   % with an average of 29 %. At extreme peaks (hindcast HA $\geq$ 30,000 km^2), compared to the MAPB by GLMzip3 (29 %) and

387   by GAMqsp3 (28 %), the statistic decreases to 25 % by the ensemble model. The ensemble model provides a higher accuracy

388   in peak forecast given minor sacrifices in overall performance.

389   **3.4 Application to Global Forecast Products (HYCOM)**

390   The power of the prediction model relies on the availability of the forecast of predictors. In this section, we discuss the model's

391   transferability using an independent global ocean product. The Global Ocean Forecasting System (GOFS) 3.1 provides global

392   daily analysis products and an eight-day forecast in a daily interval with a horizontal resolution of 1/12 °. The products

393   (hereafter referred to as HYCOM-derived products) are derived by a 41-layer HYCOM global model (Bleck and Boudra, 1981;

394   Bleck, 2002) with data assimilated via the Navy Coupled Ocean Data Assimilation (NCODA) system (Cummings, 2005;

395   Cummings and Smedstad, 2013). The Mississippi River total nitrate+nitrite loadings are provided by USGS NWIS as described

396   in section 2.1.2. Daily HYCOM-derived hydrodynamics and USGS river nitrogen loads from 1 January 2007 to 26 August

397   2020 are used to reconstruct predictors of PEA, SOCalt, and DCP_{Temp}. Relationships of ROMS-derived and HYCOM-derived

398   predictors are examined in Figure 6. The magnitudes of HYCOM-derived SOCalt and DCP_{Temp} match up with the

399   corresponding ROMS-derived predictors, respectively, although HYCOM-derived predictors are found slightly greater.

400   Simple linear regression for these predictors illustrates that the linear relationships between the ROMS and HYCOM products

401   are significant with the R^2 ranging from 0.94 to 0.96. The intercept terms are at least one-order smaller than the magnitudes of

402   corresponding predictors. Therefore, the HYCOM global products are deemed to agree with the ROMS hindcasts for SOCalt

403   and DCP_{Temp}. Nevertheless, the magnitude of HYCOM-derived PEA is found much lower than the ROMS-derived PEA

404 (Figure 6a). Simple linear regression indicates a significant linear relationship between the natural log transformation of PEA

405 from the two datasets (R^2=0.66).

406

407 At land-sea interfaces, the HYCOM global model is forced by monthly riverine discharges, which weaken the model

408 performance in coastal regions. The hydrodynamics in the LaTex Shelf is highly affected by the freshwater and momentum

409 from the Mississippi and the Atchafalaya Rivers. Monthly river forcings in HYCOM are essentially weaker than daily forcings

410 used in our ROMS setups and can result in a less stratified water column (i.e., lower PEA). Therefore, it is necessary to scale

411 the magnitude of HYCOM-derived PEA to that of the ROMS hindcast. It can be achieved by using the natural log

412 transformation and simple linear regression as discussed. We then adjusted HYCOM-derived PEA but kept the HYCOM-

413 derived SOCalt and DCP$_{Temp}$ unchanged before the application of the ensemble model.

414

415 The Bagging approach is implemented again to assess the performances of the ensemble model. During each iteration

416 (N=1,000), the GLMzip3 and GAMqsp3 are trained using the ROMS training set and then applied to the adjusted HYCOM-

417 derived predictors for HA prediction from 1 January 2012 to 26 August 2020 (Figure 7a). The ensemble method provides

418 averages and 95 % PIs of predicted HA blending Bagging results by GLMzip3 and GAMqsp3. Compared to observed HA by

419 mid-summer Shelf-wide cruises, the ensemble model fails in the summers of 2013, 2014, 2017, and 2018, but provides accurate

420 predictions in other summers. The width of 95 % PI is larger during high HA periods suggesting less stability in the HA peak

421 forecast. The overall performance is barely acceptable with an R^2 of 0.4242, an RMSE of 5,088 km^2, and a SI of 38%. The

422 bias against the observations can be ascribed to the HYCOM's failures in reproducing the shelf hydrodynamics, although

423 HYCOM-derived predictors are adjusted before being applied to the model (Figure 6a). We noticed that among the three

424 variables, HYCOM-derived PEA exhibits the largest deviation from that generated by ROMS. We then applied the model

425 using ROMS-derived PEA, HYCOM-derived SOCalt, and HYCOM-derived DCP$_{Temp}$ (Figure 7b). The performance of the

426 ensemble model was largely enhanced with a higher R^2 (0.9255), a much lower RMSE (3,751 km^2), and a lower SI (28%)

427 compared to that using pure HYCOM products. These results indicate that the ensemble model can produce a highly accurate

428 prediction for HA summer peaks once water stratification is well resolved. Instead of using monthly river forcings, the

429 HYCOM model may possibly resolve the shelf hydrodynamics by utilizing daily river discharges of the Mississippi and the

430 Atchafalaya Rivers.

431
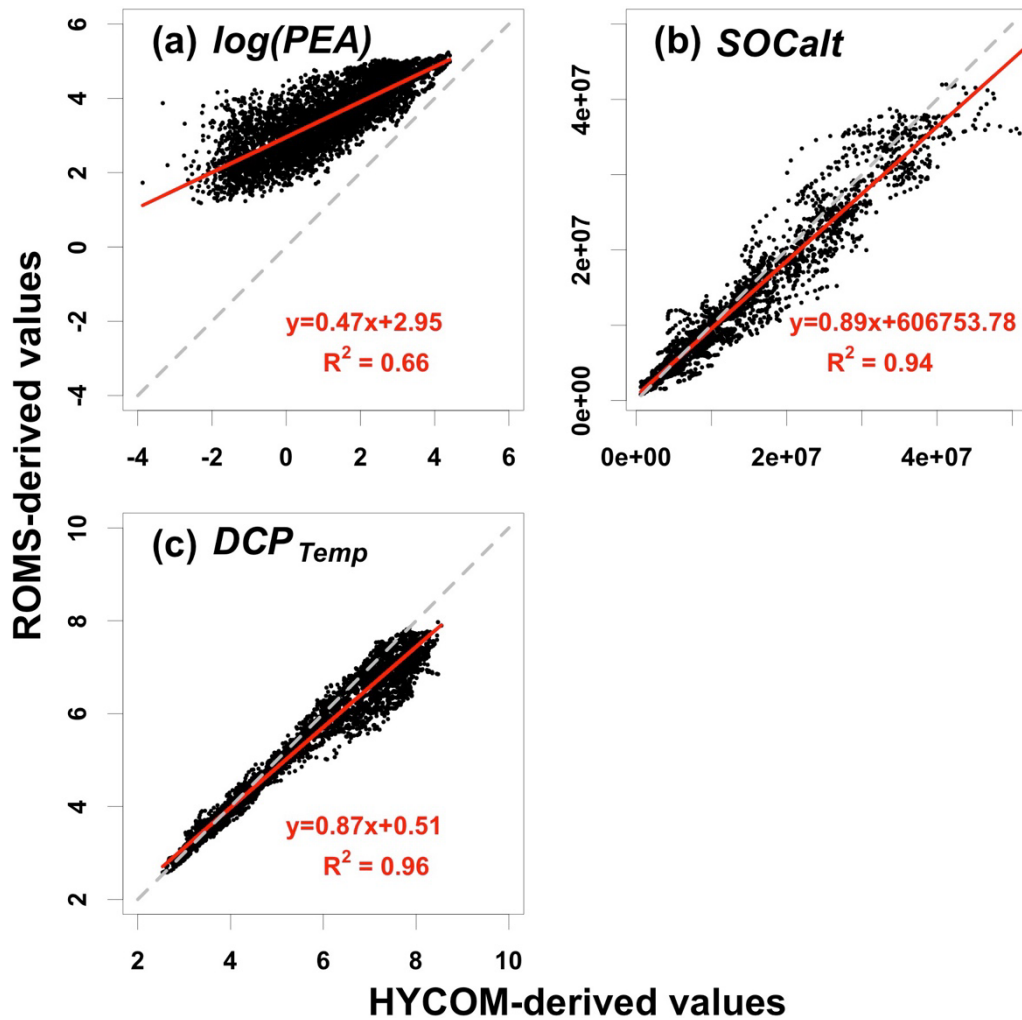
Figure 6. Scatter plots of (a) log(PEA) (unit: log (J m^{-3})), (b) SOCalt (unit: mmol s^{-1}), and (c) DCP$_{Temp}$ (unit: 1) between ROMS and HYCOM simulations. Note that the solid red lines represent linear regression lines, while the dashed grey lines are diagonals with a slope of 1 and an intercept of 0. Daily data compared are from 2007 to 2020.

435
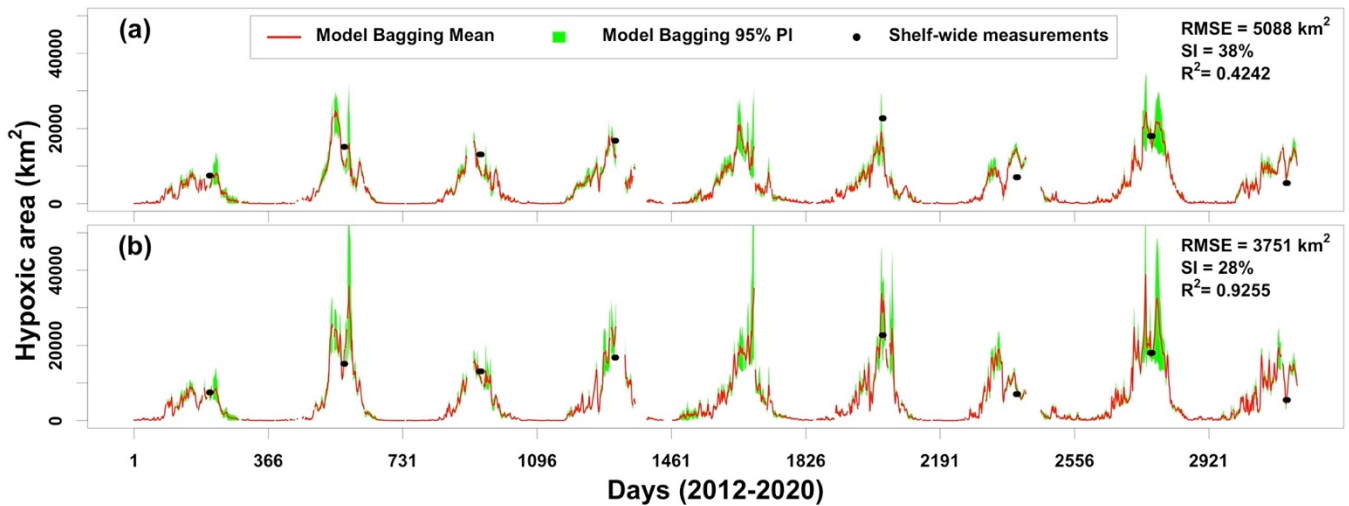
Figure 7. Comparisons of daily predicted HA by ensemble model ((GLMzip3+GAMqsp3)/2) when applied to adjusted HYCOM products and Shelf-wide measurements from 2012 to 2020. Model results shown in (a) are predicted using pure HYCOM-derived products (i.e., PEA, SOCalt, and DCP_{Temp}), while those in (b) are predicted by ROMS-derived PEA, HYCOM-derived SOCalt, and HYCOM-derived DCP_{Temp}. Discontinuity of the predictions is due to the lack of riverine nitrate+nitrite records at site USGS 07374000 in the Mississippi River.

4 Discussion

4.1 Model performance evaluation

To further assess the robustness of our model, we reviewed a suite of existing forecast models that are transitioned operationally (in early June) to the NOAA ensemble forecast for each summer (data sources are listed in Table 4). Using the ROMS-derived predictors, daily HA predictions during the Shelf-wide cruises periods are averaged for each summer from 2012 to 2020 and are compared to the cruise observations. As shown in Figure 8a, our model predictions fit well with the Shelf-wide observation for summers with or without strong windy events prior to the cruises. Other seasonal forecast models have similar performances to our model in fair-weather summers (i.e., 2012, 2014, 2015, and 2017) but fail to produce an accurate forecast for several summers with strong wind conditions (i.e., 2018 and 2020). Percentage differences between predictions and observations (Figure 8b) also emphasize the superiority of our model with the percentages ranging from -24 % to 7 % for fair-weather summers and from 7 % to 35 % for summers with strong wind or storms. All models underestimate or overestimate observed HA in fair weather summers, but overestimate HA in windy summers. Our model provides the most accurate overall performance with the highest R^2 (0.9200, N=8), the lowest RMSE (2,005 km^2, N=8), the lowest SI (15 %, N=8), and the lowest MAPB (18 %, N=8) among all models (Table 4). The multiple linear regression model developed by Forrest et al. (2011) provides the second optimal prediction. For fair-weather summers, the NOAA ensemble predictions produce the best estimation of the observed HA with a MAPB of 9 % (N=4), while our model results rank the second (15 %, N=4). However,

19

457 our model performs the best in windy summers with a MAPB of 18 % (N=4), while other models produce a MAPB from 33 %
458 to 74 %.

459

460 Models developed by Turner et al. (2006, 2008, 2012) and Laurent and Fennel (2019) are calibrated on May nitrate or
461 nitrate+nitrite loads from the Mississippi–Atchafalaya River Basin, assuming that the predicted HA in summers are under fair
462 weather. It is expected that models excluding wind effects can hardly produce accurate forecasts during summers with strong
463 winds or storms. Wind mixing effects on HA are considered in reaeration by introducing a wind stress term in the mechanistic
464 model (Obenour et al., 2015), while in the Bayesian model by Scavia et al (2013), the wind effects are considered indirectly
465 via an estimation based on current velocity and the reaeration rate given different wind conditions (i.e., fair weather, strong
466 westerly winds, and storms). However, as shown in Figure 1a, PEA_{wind}, which can also be interpreted as wind power, is found
467 poorly correlated to daily HA (R=-0.2458) compared to other highly correlated predictors and is dropped out of the candidate
468 list by the best subset searching approach. Forrest et al., (2011) also found that monthly wind power is not significantly
469 correlated to summer HA due to the short timescales of strong wind events. Therefore, the wind mixing effects considered by
470 Obenour et al (2015) and Scavia et al (2013) have limited contribution to the prediction of the interannual variability of the
471 HA. Indeed, our model construction process indicates that wind mixing, freshwater plume, and water temperature jointly
472 control the water stratification and vertical mixing, which directly modulates the reoxygenation of shelf water. PEA can serve
473 better in representing such effects rather than by wind speed or wind power alone. The daily PEA is significantly correlated to
474 daily HA (R=0.8178, $p<0.01$; Figure 1a) while the nonlinear effects of PEA cannot be neglected (Figure 5a). Therefore, an
475 accurate forecast of shelf hydrodynamics is critical for a robust summer HA prediction.

476
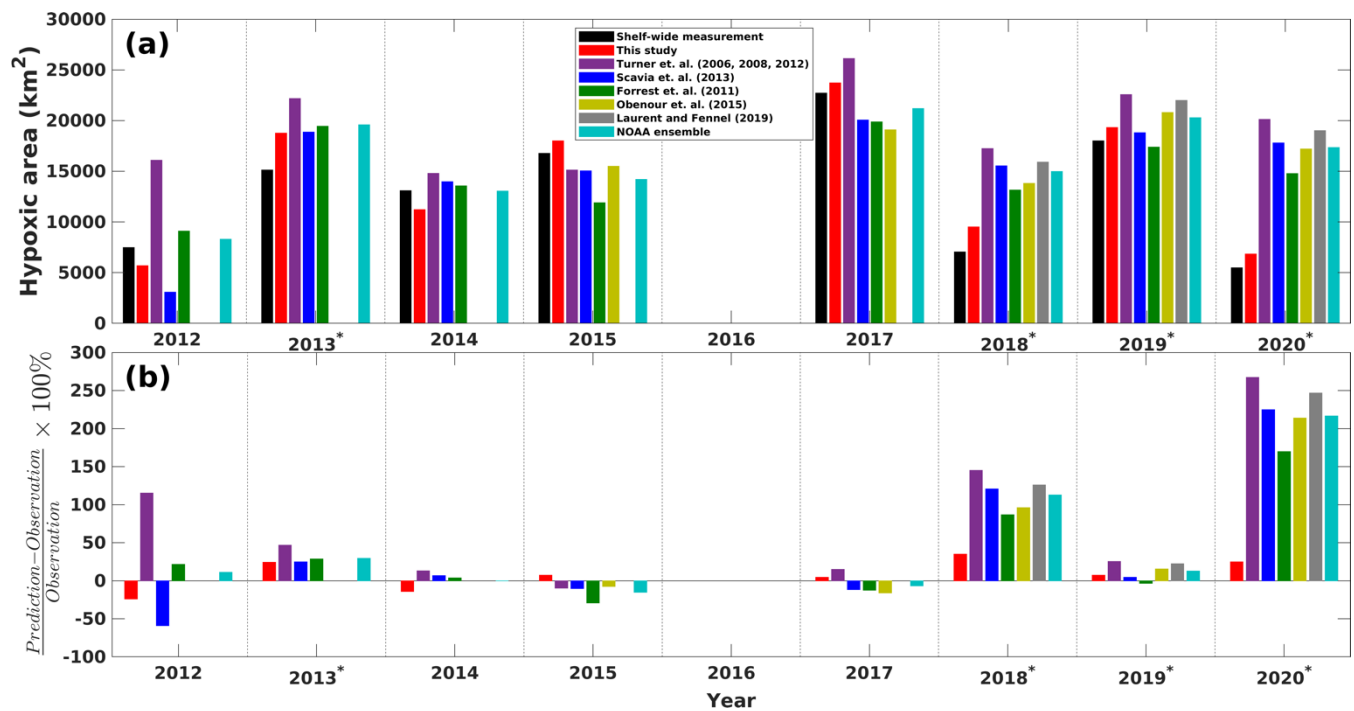
Figure 8. (a) Comparisons of Shelf-wide measured and the best estimates of model predicted HA during the Shelf-wide cruise periods. (b) Percentage differences between different model predictions and Shelf-wide measurements. The superscript asterisks indicate high-wind years prior to the cruises.

480

Table 4 Statistics comparisons between model predictions and the Shelf-wide measurements. The R^2s for predictions by Obenour et al. (2015) and Laurent and Fennel (2019) are not given since the numbers of available records are small (N=5 and 3, respectively). Numbers in paratheses indicate the numbers of compared records. Underscript "fair" and "windy" indicate that averages of corresponding statistics are conducted for fair-weather and windy summers, respectively.

	This study	Turner et al. (2006, 2008, 2012)	Scavia et al. (2013)	Forrest et al. (2011)	Obenour et al. (2015)	Laurent and Fennel (2019)	NOAA ensemble
R^2	0.9200 (N=8)	0.3017 (N=8)	0.2577 (N=8)	0.4061 (N=8)	– (N=5)	– (N=3)	0.3566 (N=8)
RMSE (km)	2005 (N=8)	7750 (N=8)	5797 (N=8)	4710 (N=8)	6412 (N=5)	9614 (N=3)	5460 (N=8)
SI	15 % (N=8)	59 % (N=8)	44 % (N=8)	36 % (N=8)	46 % (N=5)	95 % (N=3)	41 % (N=8)
MAPB	18 % (N=8)	80 % (N=8)	58 % (N=8)	44 % (N=8)	70 % (N=5)	132 % (N=3)	51 % (N=8)

| MAPB$_{fair-weather}$	15 % (N=4)	46 % (N=4)	25 % (N=4)	18 % (N=4)	8 % (N=2)	– (N=0)	9 % (N=4)
MAPB$_{windy}$	18 % (N=4)	58 % (N=4)	40 % (N=4)	33 % (N=4)	43 % (N=3)	74 % (N=3)	40 % (N=4)
Data source (access in June 2022)	https://gulfhypoxia.net/ (Turner et al., 2006; 2008; 2012) http://scavia.seas.umich.edu/hypoxia-forecasts/ (Scavia et al., 2013) https://www.vims.edu/research/topics/dead_zones/forecasts/gom/index.php (Forrest et al., 2011) https://obenour.wordpress.ncsu.edu/news/ (Obenour et al., 2015) https://memg.ocean.dal.ca/news/ (Laurent and Fennel, 2019), https://www.noaa.gov/news (NOAA ensemble)

485

4.2 Task force nutrient reduction

In this section we assess the effects of nutrient reductions on HA using our model. Since 2001, the Mississippi River/Gulf of Mexico Hypoxia Task Force has set up a goal of controlling the size of mid-summer hypoxic zone below 5,000 km^2 in a 5-year running average (Mississippi River/Gulf of Mexico Watershed Nutrient Task Force, 2001; 2008) by reducing riverine nutrient loads. Because the monthly riverine silicate, phosphate, and nitrate+nitrite loads are highly correlated (Table A1), here we refer to nitrogen load (the only nutrient that has daily measurements) as the proxy for all riverine nutrients. The averaged summer HA during the Shelf-wide cruises in the most recent five years (2015, 2107, 2018, 2019, and 2020) are calculated with different nutrient reduction scenarios and are shown in Figure 9. The PEA, bottom temperature, and river discharges are unchanged, while the SOCalt is altered by reducing the nutrient concentration from 5% to 90%. The averaged observed HA is 14,000 km^2, while the averaged prediction by our ensemble model is 15,478 km^2, which is 11 % greater than the observation. As a leading time of 44 days (Figure A3a) is prescribed in SOCalt prior to Shelf-wide summer cruises in mid–late July, reduction strategies are applied to mid-June nutrient loads rather than May loads in our model. The monthly averaged total nitrogen loads for the 1980–1996 summers (April, May, and June) are 1.96×10^8 kg/month (Battaglin et al., 2010). It is comparable to the June-mean total nitrogen load (1.6×10^8 kg month^{-1}) for the 2015–2020 period. We find that a 92 % reduction, which corresponds to a total nitrogen load of 5.5×10^5 kg day^{-1} or 1.6×10^7 kg month^{-1}, is needed for the mid-June nutrient loads to achieve the goal of a 5,000 km^2 HA.

The recommended reduction strategy by our model is much more demanding than that by other models (Scavia et al., 2013; Obenour et al., 2015; Turner et al., 2012; Laurent and Fennel, 2019), which recommend a load reduction of 52 %–58 % related to the 1980–1996 average (Scavia et al., 2017). A recommendation of 92 % reduction is closed to that by Forrest et al. (2011) (80 %) when the coastal westerlies from 15 June to 15 July were considered in their regression model. Since water stratification is attributed to not only wind mixing effects but also effects from other physical processes (e.g., riverine freshwater transports

508 and surface heating), models developed based solely on May nutrient loads (Turner et al., 2012; Laurent and Fennel, 2019) or

509 nutrient loads and wind mixing (Scavia et al., 2013; Obenour et al., 2015) fail to capture water stratification's contribution to

510 hypoxia development. If a model considers the variability of HA to rely highly on the nutrient loads, then a moderate decrease

511 in nutrient loads would result in a substantial HA reduction. For further illustration, we re-ran the model without consideration

512 of the PEA (i.e., use DCP_{Temp} and SOCalt or use only SOCalt). Model results show a substantial shrink of HA with moderately

513 reduced riverine nitrogen loads (Figure 9). In details, if only DCP_{Temp} and SOCalt are used as the predictors, a nutrient reduction

514 by 60 % will satisfy the 5000 km² HA goal. And if we only use SOCalt as the predictor, then a 55 % in reduction is sufficient.

515 These results highlight the importance of considering PEA in HA predictions.
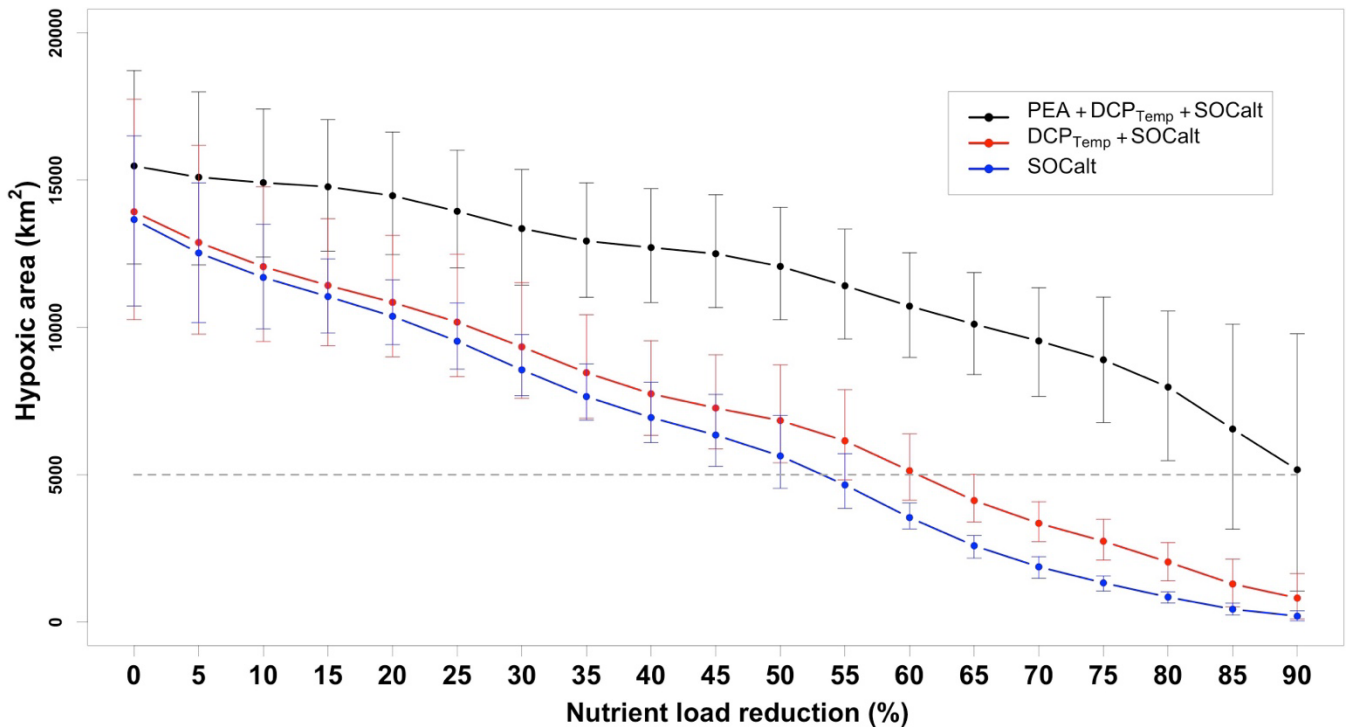
516

517 **Figure 9 2015–2020 mean (except 2016) of predicted HA in scenarios of different nutrient load reduction strategies given different**
518 **sets of predictors considered. Predictions by the ensemble model are conducted individually for the Shelf-wide cruise periods in**
519 **different summers and averaged from 2015 to 2020. Horizontal bars indicate ranges of 95 % PIs. Grey dashed lines represent the**
520 **goal of 5,000 km² set by the Mississippi River/Gulf of Mexico Hypoxia Task Force. Note here nutrient reduction percentages are**
521 **referred to mid-June nutrient loads in corresponding years.**

522 **5 Conclusion**

523 In this study, we present a novel HA forecast model for the LaTex Shelf using statistical analysis. The model is trained using

524 numeric simulations from 1 January 2007 to 26 August 2020 by a 3-dimensional coupled hydrodynamic–biogeochemical

525 model (ROMS). Multiple GLMs (regular Poisson GLMs, quasi-Poisson GLMs, negative binomial GLMs, zero-inflated

526 Poisson GLMs, and zero-inflated negative binomial GLMs) and GAMs (regular Poisson GAMs, quasi-Poisson GAMs, and

23

regular negative binomial GAMs) are assessed for HA predictions. Comparisons of model prediction performance illustrate that an ensemble model combing the prediction efforts of a zero-inflated Poisson GLM (GLMzip3) and a quasi-Poisson GAM (GAMqsp3) provides the most accurate HA forecast with PEA, SOCalt, and DCP$_{Temp}$ as predictors. The ensemble model is capable of explaining up to 77 % of the total variability of the hindcast HA and also provides a low RMSE of 3,256 km^2 and low MAPBs for overall (29 %) and peak predictions (25 %) when compared to the daily ROMS hindcasts.

We then applied the hydrodynamics field generated by a global model (HYCOM, GOFS 3.1) and performed a HA hindcast for the period from 1 January 2012 to 26 August 2020. The overall performance is barely acceptable with an R^2 of 0.4242, an RMSE of 5,088 km^2, and a SI of 38 % against the Shelf-wide summer cruise observations, largely due to HYCOM's relatively poor representation of shelf stratification. A substitution of ROMS-derived PEA led to a pronounced improvement with an R^2 of 0.9255, an RMSE of 3,751 km^2, and an SI of 28 %.

The ensemble model also provides an efficient yet more robust summer HA forecast than existing HA forecast models. Comparing against the Shelf-wide cruise observations, our model provides a high R^2 (0.9200 vs 0.2577–0.4061 by existing forecast models, same comparison hereinafter), a low RMSE (2,005 km^2 vs 4,710–9,614 km^2), a low SI (15 % vs 36 %–95 %), low MAPBs for overall (18 % vs 44 %–132 %), fair-weather summers (15 % vs 8 %–46 %), and windy summers (18 % vs 33 %–74 %) predictions. Sensitivity tests are conducted and suggests that a 92 % reduction in riverine nutrients related to the 1980–1996 summer average is required to meet the goal of a 5,000 km^2 HA. These results highlight the importance of considering PEA in HA prediction.

Code/Data availability: Model data is available at the LSU mass storage system and details are on the webpage of the Coupled Ocean Modeling Group at LSU (https://faculty.lsu.edu/zxue/). Data requests can be sent to the corresponding author via this webpage.

Author contribution: Bin Li and Z. George Xue designed the experiments and Yanda Ou carried them out. Yanda Ou developed the model code and performed the simulations. Yanda Ou, Bin Li, and Z. George Xue prepared the manuscript.

Competing interests: The authors declare that they have no conflict of interest.

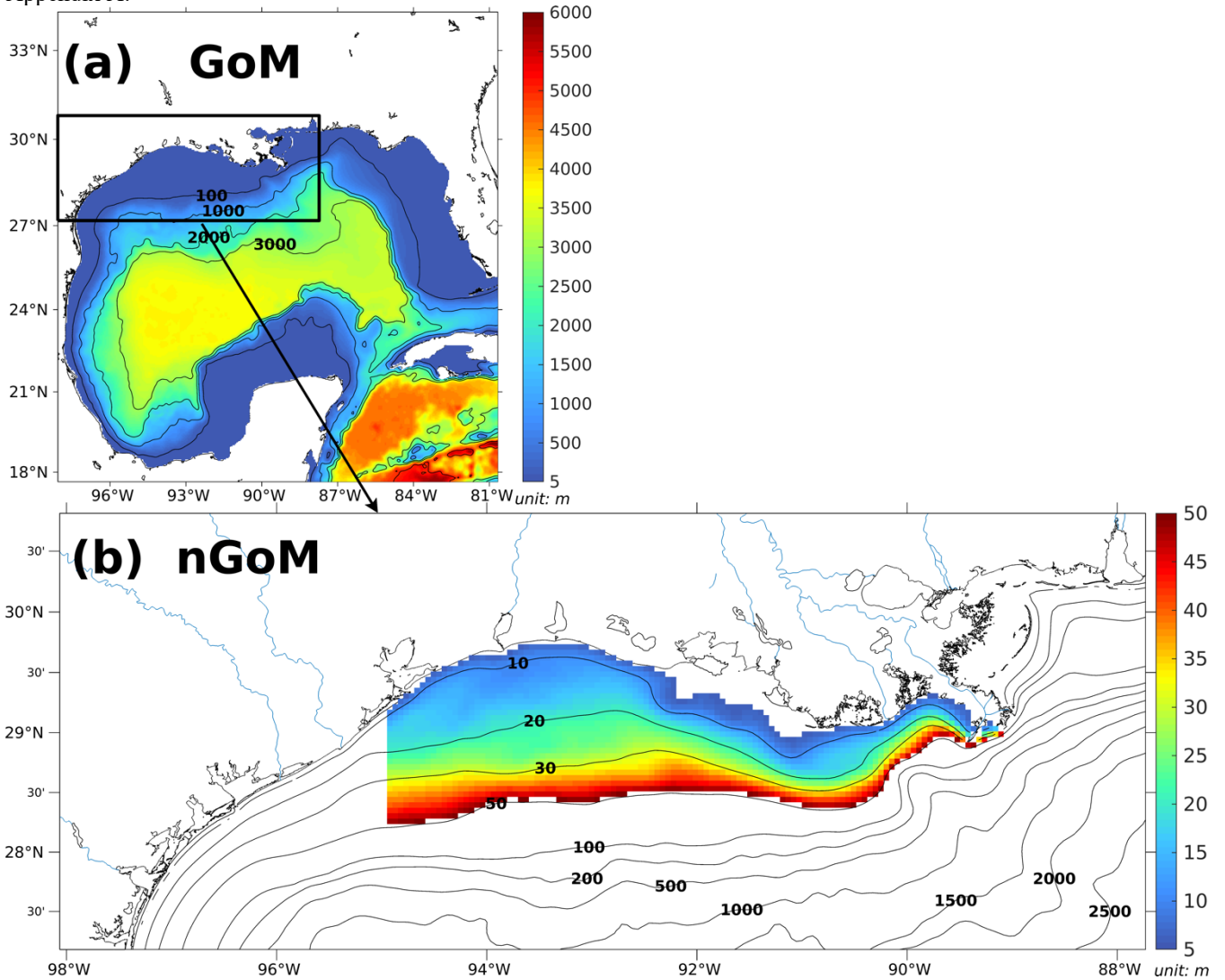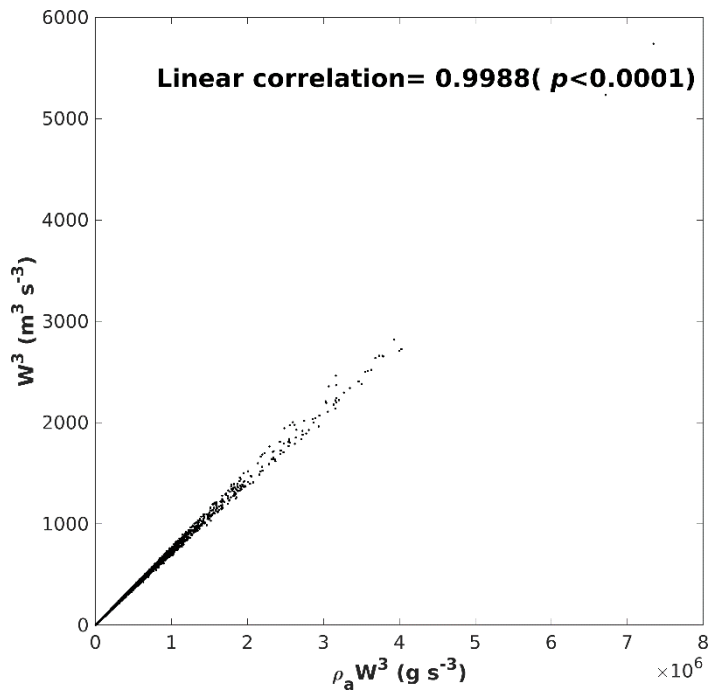562   Appendix A:

563
564   **Figure A1 (a) Bathymetry of the entire domain of the Gulf–COAWST described in the accompanying study (Part I) and (b) zoom-**
565   **in bathymetry plot of the northern Gulf of Mexico (nGoM). The range of bathymetry of the color shaded area in (b) is from 6 to 50**
566   **m, over which the regional averages of parameters are conducted.**

567

Figure A2. A scatter plot of $\rho_a W^3$ against W^3 and their linear correlation.

569 Table A1 A correlation matrix of monthly mean inorganic nutrient loads by the Mississippi River and the Atchafalaya River from
570 2007 to 2020. Correlation coefficients shown are all significant ($p<0.001$).

	Mississippi nitrate+nitrite	Atchafalaya nitrate+nitrite	Mississippi phosphate	Atchafalaya phosphate	Mississippi silicate	Atchafalaya silicate
Mississippi nitrate+nitrite	1					
Atchafalaya nitrate+nitrite	0.9207	1				
Mississippi phosphate	0.8258	0.7551	1			
Atchafalaya phosphate	0.7576	0.7764	0.9308	1		
Mississippi silicate	0.8511	0.7770	0.8664	0.7972	1	
Atchafalaya silicate	0.7989	0.7781	0.8147	0.7942	0.9673	1

571

26
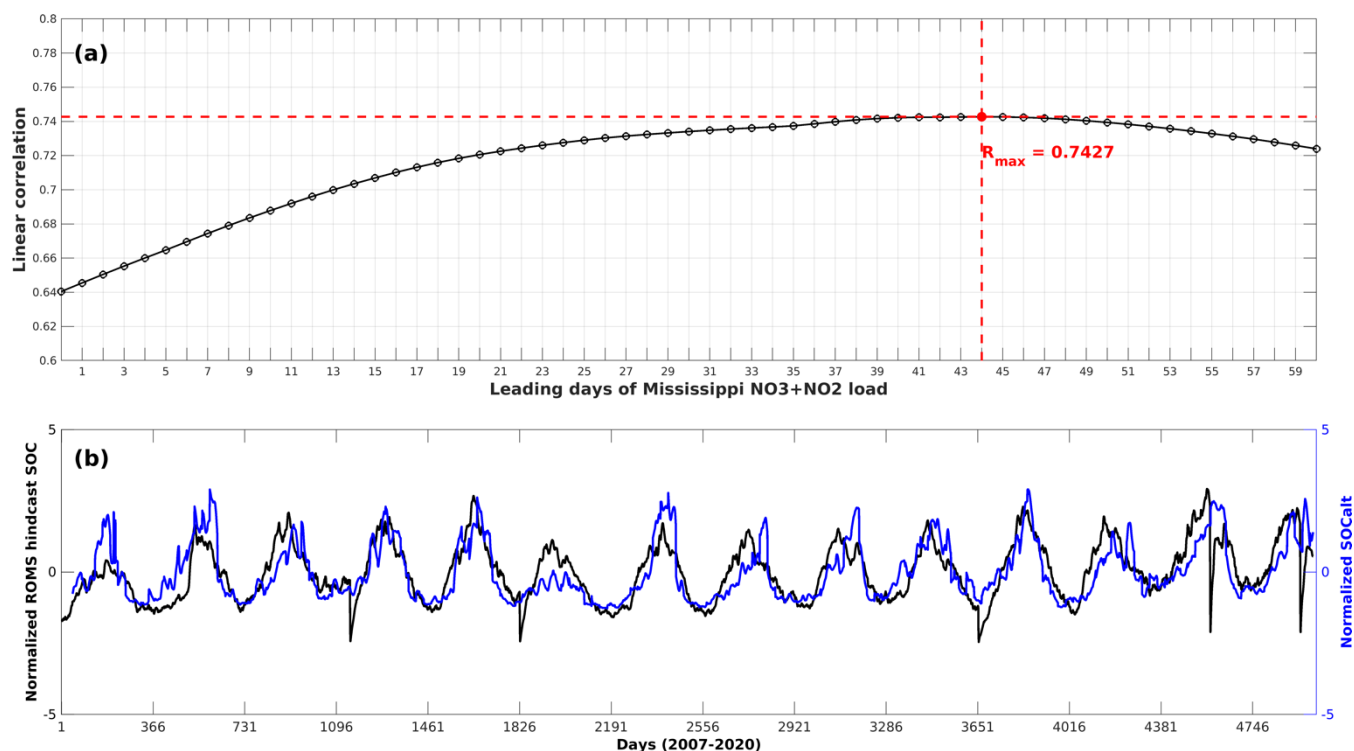
Figure A3. (a) Lead/lag correlation coefficients between ROMS hindcast daily SOC and SOCalt (= Mississippi River inorganic nitrogen loads $\cdot$ e$^{0.0693T_b}$) with the Mississippi nitrogen loads leading by different days; **(b)** daily time series of ROMS hindcast SOC and SOCalt when the Mississippi nitrogen loads leading by 44 days. The time series are regional average results over the LaTex Shelf and are normalized.

Reference

Battaglin, W. A., Aulenbach, B. T., Vecchia, A., and Buxton, H. T.: Changes in streamflow and the flux of nutrients in the Mississippi-Atchafalaya River Basin, USA, 1980-2007, Scientific Investigations Report, Reston, VA, https://doi.org/10.3133/sir20095164, 2010.

Bianchi, T. S., DiMarco, S. F., Cowan, J. H., Hetland, R. D., Chapman, P., Day, J. W., and Allison, M. A.: The science of hypoxia in the northern Gulf of Mexico: A review, Sci. Total Environ., 408, 1471–1484, https://doi.org/10.1016/j.scitotenv.2009.11.047, 2010.

Bleck, R.: An oceanic general circulation model framed in hybrid isopycnic-Cartesian coordinates, Ocean Model., 4, 55–88, https://doi.org/10.1016/S1463-5003(01)00012-9, 2002.

Bleck, R. and Boudra, D. B.: Initial testing of a numerical ocean circulation model using a hybrid (quasi-isopycnic) vertical coordinate, J. Phys. Oceanogr., 11, 755–770, https://doi.org/https://doi.org/10.1175/1520-0485(1981)011<0755:ITOANO>2.0.CO;2, 1981.

Chesney, E. J. and Baltz, D. M.: The effects of hypoxia on the northern Gulf of Mexico Coastal Ecosystem: A fisheries perspective, in: Coastal Hypoxia: Consequences for Living Resources and Ecosystems, American Geophysical Union, 321–354, https://doi.org/10.1029/CE058p0321, 2001.

Conley, D. J., Paerl, H. W., Howarth, R. W., Boesch, D. F., Seitzinger, S. P., Havens, K. E., Lancelot, C., and Likens, G. E.: Controlling Eutrophication: Nitrogen and Phosphorus, Science (80-.)., 323, 1014–1015, https://doi.org/10.1126/science.1167755, 2009.

Craig, J. K.: Aggregation on the edge: Effects of hypoxia avoidance on the spatial distribution of brown shrimp and demersal fishes in the Northern Gulf of Mexico, Mar. Ecol. Prog. Ser., 445, 75–95, https://doi.org/10.3354/meps09437, 2012.

Craig, J. K. and Bosman, S. H.: Small Spatial Scale Variation in Fish Assemblage Structure in the Vicinity of the Northwestern Gulf of Mexico Hypoxic Zone, 36, 268–285, https://doi.org/10.1007/s12237-012-9577-9, 2013.

Craig, J. K. and Crowder, L. B.: Hypoxia-induced habitat shifts and energetic consequences in Atlantic croaker and brown shrimp on the Gulf of Mexico shelf, Mar. Ecol. Prog. Ser., 294, 79–94, https://doi.org/10.3354/meps294079, 2005.

Cummings, J. A.: Operational multivariate ocean data assimilation, Q. J. R. Meteorol. Soc., 131, 3583–3604, https://doi.org/10.1256/qj.05.105, 2005.

Cummings, J. A. and Smedstad, O. M.: Variational Data Assimilation for the Global Ocean, in: Data Assimilation for Atmospheric, Oceanic and Hydrologic Applications, vol. II, edited by: Park, S. K. and Xu, L., Springer Berlin Heidelberg, 303–343, https://doi.org/10.1007/978-3-642-35088-7_13, 2013.

Feng, Y., Fennel, K., Jackson, G. A., DiMarco, S. F., and Hetland, R. D.: A model study of the response of hypoxia to upwelling-favorable wind on the northern Gulf of Mexico shelf, J. Mar. Syst., 131, 63–73, https://doi.org/10.1016/j.jmarsys.2013.11.009, 2014.

Fennel, K., Hetland, R., Feng, Y., and Dimarco, S.: A coupled physical-biological model of the Northern Gulf of Mexico shelf: Model description, validation and analysis of phytoplankton variability, 8, 1881–1899, https://doi.org/10.5194/bg-8-1881-2011, 2011.

Fennel, K., Hu, J., Laurent, A., Marta-Almeida, M., and Hetland, R.: Sensitivity of hypoxia predictions for the northern Gulf of Mexico to sediment oxygen consumption and model nesting, J. Geophys. Res. Ocean., 118, 990–1002, https://doi.org/10.1002/jgrc.20077, 2013.

Fennel, K., Laurent, A., Hetland, R., Justic, D., Ko, D. S., Lehrter, J., Murrell, M., Wang, L., Yu, L., and Zhang, W.: Effects of model physics on hypoxia simulations for the northern Gulf of Mexico: A model intercomparison, J. Geophys. Res. Ocean., 121, 5731–5750, https://doi.org/10.1002/2015JC011516, 2016.

Forrest, D. R., Hetland, R. D., and DiMarco, S. F.: Multivariable statistical regression models of the areal extent of hypoxia over the Texas-Louisiana continental shelf, Environ. Res. Lett., 6, 045002, https://doi.org/10.1088/1748-9326/6/4/045002, 2011.

Del Giudice, D., Matli, V. R. R., and Obenour, D. R.: Bayesian mechanistic modeling characterizes Gulf of Mexico hypoxia: 1968–2016 and future scenarios, Ecol. Appl., 30, 1–14, https://doi.org/10.1002/eap.2032, 2020.

Hazen, E. L., Craig, J. K., Good, C. P., and Crowder, L. B.: Vertical distribution of fish biomass in hypoxic waters on the gulf of Mexico shelf, Mar. Ecol. Prog. Ser., 375, 195–207, https://doi.org/10.3354/meps07791, 2009.

Hetland, R. D. and DiMarco, S. F.: How does the character of oxygen demand control the structure of hypoxia on the Texas-Louisiana continental shelf?, J. Mar. Syst., 70, 49–62, https://doi.org/10.1016/j.jmarsys.2007.03.002, 2008.

Jackman, S.: pscl: Classes and Methods for R Developed in the Political Science Computational Laboratory, https://github.com/atahk/pscl/, 2020.

629 Justić, D. and Wang, L.: Assessing temporal and spatial variability of hypoxia over the inner Louisiana-upper Texas shelf:
630 Application of an unstructured-grid three-dimensional coupled hydrodynamic-water quality model, Cont. Shelf Res., 72, 163–
631 179, https://doi.org/10.1016/j.csr.2013.08.006, 2014.

632 Katin, A., Del Giudice, D., and Obenour, D. R.: Temporally resolved coastal hypoxia forecasting and uncertainty assessment
633 via Bayesian mechanistic modeling, Hydrol. Earth Syst. Sci., 26, 1131–1143, https://doi.org/10.5194/hess-26-1131-2022,
634 2022.

635 LaBone, E., Rose, K., Justic, D., Huang, H., and Wang, L.: Effects of spatial variability on the exposure of fish to hypoxia: a
636 modeling analysis for the Gulf of Mexico, Biogeosciences Discuss., 1–35, https://doi.org/10.5194/bg-2020-51, 2020.

637 Lambert, D.: Zero-inflated poisson regression, with an application to defects in manufacturing, 34, 1–14,
638 https://doi.org/10.1080/00401706.1992.10485228, 1992.

639 Laurent, A. and Fennel, K.: Time-Evolving, Spatially Explicit Forecasts of the Northern Gulf of Mexico Hypoxic Zone,
640 Environ. Sci. Technol., 53, 14449–14458, https://doi.org/10.1021/acs.est.9b05790, 2019.

641 Laurent, A., Fennel, K., Ko, D. S., and Lehrter, J.: Climate change projected to exacerbate impacts of coastal Eutrophication
642 in the Northern Gulf of Mexico, J. Geophys. Res. Ocean., 123, 3408–3426, https://doi.org/10.1002/2017JC013583, 2018.

643 Matli, V. R. R., Fang, S., Guinness, J., Rabalais, N. N., Craig, J. K., and Obenour, D. R.: Space-Time Geostatistical Assessment
644 of Hypoxia in the Northern Gulf of Mexico, Environ. Sci. Technol., 52, 12484–12493, https://doi.org/10.1021/acs.est.8b03474,
645 2018.

646 Mattern, J. P., Fennel, K., and Dowd, M.: Sensitivity and uncertainty analysis of model hypoxia estimates for the Texas-
647 Louisiana shelf, J. Geophys. Res. Ocean., 118, 1316–1332, https://doi.org/10.1002/jgrc.20130, 2013.

648 McCarthy, M. J., Carini, S. A., Liu, Z., Ostrom, N. E., and Gardner, W. S.: Oxygen consumption in the water column and
649 sediments of the northern Gulf of Mexico hypoxic zone, Estuar. Coast. Shelf Sci., 123, 46–53,
650 https://doi.org/10.1016/j.ecss.2013.02.019, 2013.

651 Mississippi River/Gulf of Mexico Watershed Nutrient Task Force: Action Plan for Reducing, Mitigating, and Controlling
652 Hypoxia in the Northern Gulf of Mexico, Washington,DC., 2001.

653 Mississippi River/Gulf of Mexico Watershed Nutrient Task Force: Gulf Hypoxia Action Plan 2008 for Reducing, Mitigating,
654 and Controlling Hypoxia in the Northern Gulf of Mexico and Improving Water Quality in the Mississippi River Basin,
655 Washington,DC., 2008.

656 Monteith, J. and Unsworth, M.: Principles of environmental physics: plants, animals, and the atmosphere, 4th ed., Academic
657 Press, https://doi.org/https://doi.org/10.1016/C2010-0-66393-0, 2014.

658 Murray, F. W.: On the Computation of Saturation Vapor Pressure, J. Appl. Meteorol. Climatol., 6, 203–204,
659 https://doi.org/https://doi.org/10.1175/1520-0450(1967)006<0203:OTCOSV>2.0.CO;2, 1967.

660 Murrell, M. C. and Lehrter, J. C.: Sediment and Lower Water Column Oxygen Consumption in the Seasonally Hypoxic Region
661 of the Louisiana Continental Shelf, 34, 912–924, https://doi.org/10.1007/s12237-010-9351-9, 2011.

662 de Mutsert, K., Steenbeek, J., Lewis, K., Buszowski, J., Cowan, J. H., and Christensen, V.: Exploring effects of hypoxia on
663 fish and fisheries in the northern Gulf of Mexico using a dynamic spatially explicit ecosystem model, Ecol. Modell., 331, 142–
664 150, https://doi.org/10.1016/j.ecolmodel.2015.10.013, 2016.

665 Obenour, D. R., Michalak, A. M., and Scavia, D.: Assessing biophysical controls on Gulf of Mexico hypoxia through

666   probabilistic modeling, Ecol. Appl., 25, 492–505, https://doi.org/10.1890/13-2257.1, 2015.

667   Picard, A., Davis, R. S., Gläser, M., and Fujii, K.: Revised formula for the density of moist air (CIPM-2007), 45, 149–155,
668   https://doi.org/10.1088/0026-1394/45/2/004, 2008.

669   Purcell, K. M., Craig, J. K., Nance, J. M., Smith, M. D., and Bennear, L. S.: Fleet behavior is responsive to a large-scale
670   environmental disturbance: Hypoxia effects on the spatial dynamics of the northern Gulf of Mexico shrimp fishery,
671   https://doi.org/10.1371/journal.pone.0183032, 2017.

672   Rabalais, N. N. and Baustian, M. M.: Historical Shifts in Benthic Infaunal Diversity in the Northern Gulf of Mexico since the
673   Appearance of Seasonally Severe Hypoxia, 12, https://doi.org/10.3390/d12020049, 2020.

674   Rabalais, N. N. and Turner, R. E.: Gulf of Mexico Hypoxia: Past, Present, and Future, Limnol. Oceanogr. Bull., 28, 117–124,
675   https://doi.org/10.1002/lob.10351, 2019.

676   Rabalais, N. N., Turner, R. E., and Wiseman, W. J.: Gulf of Mexico hypoxia, a.k.a. "The dead zone," Annu. Rev. Ecol. Syst.,
677   33, 235–263, https://doi.org/10.1146/annurev.ecolsys.33.010802.150513, 2002.

678   Rabalais, N. N., Turner, R. E., Sen Gupta, B. K., Boesch, D. F., Chapman, P., and Murrell, M. C.: Hypoxia in the northern
679   Gulf of Mexico: Does the science support the plan to reduce, mitigate, and control hypoxia?, 30, 753–772,
680   https://doi.org/10.1007/BF02841332, 2007a.

681   Rabalais, N. N., Turner, R. E., Gupta, B. K. S., Platon, E., and Parsons, M. L.: Sediments tell the history of eutrophication and
682   hypoxia in the northern Gulf of Mexico, Ecol. Appl., 17, 129–143, https://doi.org/10.1890/06-0644.1, 2007b.

683   Rabotyagov, S. S., Kling, C. L., Gassman, P. W., Rabalais, N. N., and Turner, R. E.: The economics of dead zones: Causes,
684   impacts, policy challenges, and a model of the gulf of Mexico Hypoxic Zone, Rev. Environ. Econ. Policy, 8, 58–79,
685   https://doi.org/10.1093/reep/ret024, 2014.

686   Reyes, B. A., Pendergast, J. S., and Yamazaki, S.: Mammalian peripheral circadian oscillators are temperature compensated,
687   J. Biol. Rhythms, 23, 95–98, https://doi.org/10.1177/0748730407311855, 2008.

688   Saha, S., Moorthi, S., Pan, H.-L., Wu, X., Wang, J., Nadiga, S., Tripp, P., Kistler, R., Woollen, J., Behringer, D., Liu, H.,
689   Stokes, D., Grumbine, R., Gayno, G., Wang, J., Hou, Y.-T., Chuang, H.-Y., Juang, H.-M. H., Sela, J., Iredell, M., Treadon, R.,
690   Kleist, D., Van Delst, P., Keyser, D., Derber, J., Ek, M., Meng, J., Wei, H., Yang, R., Lord, S., van den Dool, H., Kumar, A.,
691   Wang, W., Long, C., Chelliah, M., Xue, Y., Huang, B., Schemm, J.-K., Ebisuzaki, W., Lin, R., Xie, P., Chen, M., Zhou, S.,
692   Higgins, W., Zou, C.-Z., Liu, Q., Chen, Y., Han, Y., Cucurull, L., Reynolds, R. W., Rutledge, G., and Goldberg, M.: NCEP
693   Climate Forecast System Reanalysis (CFSR) 6-hourly Products, January 1979 to December 2010,
694   https://doi.org/10.5065/D69K487J, 2010.

695   Saha, S., Moorthi, S., Wu, X., Wang, J., Nadiga, S., Tripp, P., Behringer, D., Hou, Y.-T., Chuang, H., Iredell, M., Ek, M.,
696   Meng, J., Yang, R., Mendez, M. P., van den Dool, H., Zhang, Q., Wang, W., Chen, M., and Becker, E.: NCEP Climate Forecast
697   System Version 2 (CFSv2) 6-hourly Products, https://doi.org/10.5065/D61C1TXF, 2011.

698   Scavia, D., Evans, M. A., and Obenour, D. R.: A scenario and forecast model for gulf of mexico hypoxic area and volume,
699   Environ. Sci. Technol., 47, 10423–10428, https://doi.org/10.1021/es4025035, 2013.

700   Scavia, D., Bertani, I., Obenour, D. R., Turner, R. E., Forrest, D. R., and Katin, A.: Ensemble modeling informs hypoxia
701   management in the northern Gulf of Mexico, Proc. Natl. Acad. Sci. U. S. A., 114, 8823–8828,
702   https://doi.org/10.1073/pnas.1705293114, 2017.

703   Siegel, A. F. and Wagner, M. R.: Chapter 12 - Multiple Regression: Predicting One Variable From Several Others, in: Practical

Business Statistics, edited by: Siegel, A. F. and Wagner, M. R., 371–431, https://doi.org/https://doi.org/10.1016/B978-0-12-820025-4.00012-9., 2022.

Simpson, J. H.: The shelf-sea fronts: implications of their existence and behaviour, Philos. Trans. R. Soc. London. Ser. A, Math. Phys. Sci., 302, 531–546, https://doi.org/10.1098/rsta.1981.0181, 1981.

Simpson, J. H. and Bowers, D.: Models of stratification and frontal movement in shelf seas, Deep Sea Res. Part A, Oceanogr. Res. Pap., 28, 727–738, https://doi.org/10.1016/0198-0149(81)90132-1, 1981.

Simpson, J. H. and Hunter, J. R.: Fronts in the Irish Sea, Nature, 250, 404–406, https://doi.org/10.1038/250404a0, 1974.

Simpson, J. H., Allen, C. M., and Morris, N. C. G.: Fronts on the Continental Shelf, J. Geophys. Res., 83, 4607–4614, https://doi.org/10.1029/JC083iC09p04607, 1978.

Smith, M. D., Asche, F., Bennear, L. S., and Oglend, A.: Spatial-dynamics of hypoxia and fisheries: The case of Gulf of Mexico brown shrimp, Mar. Resour. Econ., 29, 111–131, https://doi.org/10.1086/676826, 2014.

Turner, R. E., Rabalais, N. N., and Justic, D.: Predicting summer hypoxia in the northern Gulf of Mexico: Riverine N, P, and Si loading, Mar. Pollut. Bull., 52, 139–148, https://doi.org/10.1016/j.marpolbul.2005.08.012, 2006.

Turner, R. E., Rabalais, N. N., and Justic, D.: Gulf of Mexico hypoxia: Alternate states and a legacy, Environ. Sci. Technol., 42, 2323–2327, https://doi.org/10.1021/es071617k, 2008.

Turner, R. E., Rabalais, N. N., and Justić, D.: Predicting summer hypoxia in the northern Gulf of Mexico: Redux, Mar. Pollut. Bull., 64, 319–324, https://doi.org/10.1016/j.marpolbul.2011.11.008, 2012.

van't Hoff, J. H. and Lehfeldt, R. A.: Lectures in theoretical and physical chemistry: Part I: Chemical dynamics, London: Edward Arnold, London, 1899.

Venables, W. N. and Ripley, B. D.: Modern Applied Statistics with S, Fourth., Springer, New York, https://doi.org/10.1007/978-0-387-21706-2, 2002.

Wang, L. and Justić, D.: A modeling study of the physical processes affecting the development of seasonal hypoxia over the inner Louisiana-Texas shelf: Circulation and stratification, Cont. Shelf Res., 29, 1464–1476, https://doi.org/10.1016/j.csr.2009.03.014, 2009.

Warner, J. C., Armstrong, B., He, R., and Zambon, J. B.: Development of a Coupled Ocean-Atmosphere-Wave-Sediment Transport (COAWST) Modeling System, Ocean Model., 35, 230–244, https://doi.org/10.1016/j.ocemod.2010.07.010, 2010.

Wood, S. N.: Thin plate regression splines, J. R. Stat. Soc. Ser. B Stat. Methodol., 65, 95–114, https://doi.org/10.1111/1467-9868.00374, 2003.

Wood, S. N.: Fast stable restricted maximum likelihood and marginal likelihood estimation of semiparametric generalized linear models, J. R. Stat. Soc. Ser. B Stat. Methodol., 73, 3–36, https://doi.org/10.1111/j.1467-9868.2010.00749.x, 2011.

Yu, L., Fennel, K., and Laurent, A.: A modeling study of physical controls on hypoxia generation in the northern Gulf of Mexico, J. Geophys. Res. Ocean., 120, 5019–5039, https://doi.org/10.1002/ 2014JC010634, 2015.

Zambresky, L.: A verification study of the global WAM model, December 1987 – November 1988, 1989.

Zeileis, A., Kleiber, C., and Jackman, S.: Regression Models for Count Data in R, J. Stat. Softw., 27, https://doi.org/10.18637/jss.v027.i08, 2008.